UNIVERSIDADE FEDERAL DO RIO DE JANEIRO

INSTITUTO DE FÍSICA

Welberth Kennedy Pereira da Silva

The extended Hubbard model on a honeycomb lattice

Rio de Janeiro

Maio de 2025

UNIVERSIDADE FEDERAL DO RIO DE JANEIRO

INSTITUTO DE FÍSICA

The extended Hubbard model on a honeycomb lattice

Welberth Kennedy Pereira da Silva

Dissertação de Mestrado apresentada ao Programa de Pós-Graduação em Física do Instituto de Física da Universidade Federal do Rio de Janeiro - UFRJ, como parte dos requisitos necessários à obtenção do título de Mestre em Ciências (Física).

Orientador: Raimundo Rocha dos Santos
Coorientador: Sebastião dos Anjos Sousa-Júnior

Rio de Janeiro

Maio de 2025

The extended Hubbard model on a honeycomb lattice

Welberth Kennedy Pereira da Silva

Raimundo Rocha dos Santos
Sebastião dos Anjos Sousa-Júnior

Dissertação de Mestrado submetida ao Programa de Pós-Graduação em Física, Instituto de Física, da Universidade Federal do Rio de Janeiro – UFRJ, como parte dos requisitos necessários à obtenção do título de Mestre em Ciências (Física)

Aprovada por:

.....
Prof. Dr. Raimundo Rocha dos Santos,
IF-UFRJ (Presidente e Orientador)

.....
Dr. Sebastião dos Anjos Sousa-Júnior,
University of Houston (Coorientador)

.....
Profa. Dra. Thereza Cristina de Lacerda Paiva, UFRJ

.....
Profa. Dra. Vivian Vanessa França Henn, Unesp

Rio de Janeiro, RJ - Brasil
Maio de 2025

CIP - Catalogação na Publicação

S586t

Silva, Welberth Kennedy Pereira da
The extended Hubbard model on a honeycomb lattice / Welberth Kennedy Pereira da Silva. -- Rio de Janeiro, 2025.
64 f.

Orientador: Raimundo Rocha dos Santos.
Coorientador: Sebastião dos Anjos Sousa-Júnior.
Dissertação (mestrado) - Universidade Federal do Rio de Janeiro, Instituto de Física, Programa de Pós Graduação em Física, 2025.

1. Magnetismo. 2. Ordem de carga. 3. Superconductividade. 4. Interações estendidas. I. Rocha dos Santos, Raimundo, orient. II. dos Anjos Sousa-Júnior, Sebastião, coorient. III. Título.

Elaborado pelo Sistema de Geração Automática da UFRJ com os dados fornecidos pelo(a) autor(a), sob a responsabilidade de Miguel Romeu Amorim Neto - CRB-7/6283.

Resumo

The extended Hubbard model on a honeycomb lattice

Welberth Kennedy Pereira da Silva

Orientador: Raimundo Rocha dos Santos

Coorientador: Sebastião dos Anjos Sousa-Júnior

Resumo da Dissertação de Mestrado apresentada ao Programa de Pós-Graduação em Física do Instituto de Física da Universidade Federal do Rio de Janeiro - UFRJ, como parte dos requisitos necessários à obtenção do título de Mestre em Ciências (Física).

Estudamos o diagrama de fases do modelo de Hubbard estendido sob uma rede favo de mel (*honeycomb*) semi-preenchida por meio de simulações de Monte Carlo quântico determinantal. No modelo de Hubbard repulsivo, à temperatura nula, a transição de fase para um estado antiferromagnético ocorre apenas para um valor suficientemente forte do acoplamento local, U. No entanto, a inclusão de uma interação estendida repulsiva, V, entre férmions que ocupam orbitais de primeiros vizinhos induz uma fase com ordenamento de carga. Para interações atrativas, também identificamos uma fase supercondutora e um estado de separação de fase. Construímos um diagrama de fases completo e, para isto, calculamos os fatores de estrutura associados a diferentes ordenamentos, combinados com medidas de dupla ocupação e da média do sinal dos determinantes fermiônicos. Mostramos que a fase semimetálica forma uma região da qual as fases ordenadas são excluídas, impedindo a estabilização de uma fase supercondutora com simetria onda-d, ou seja, apenas o emparelhamento do tipo onda-s é permitido.

Keywords: Magnetismo, ordem de carga, superconductividade, interações estendidas

Abstract

The extended Hubbard model on a honeycomb lattice

Welberth Kennedy Pereira da Silva

Orientador: Raimundo Rocha dos Santos

Coorientador: Sebastião dos Anjos Sousa-Júnior

Abstract da Dissertação de Mestrado apresentada ao Programa de Pós-Graduação em Física do Instituto de Física da Universidade Federal do Rio de Janeiro - UFRJ, como parte dos requisitos necessários à obtenção do título de Mestre em Ciências (Física).

We investigate the phase diagram of the extended Hubbard model on a half-filled honeycomb lattice through determinant quantum Monte Carlo simulations. At zero temperature, the repulsive Hubbard model undergoes a transition to an antiferromagnetic state only for sufficiently strong on-site coupling, U. However, the inclusion of a repulsive extended interaction, V, between fermions in nearest-neighbor orbitals induces a charge-ordered phase. For attractive interactions, we also identify superconducting and phase-separated phases. We have determined a complete phase diagram with the aid of structure factors associated with various orderings, combined with measurements of double occupancy and the average sign of fermionic determinants. We have established that the semi-metallic phase forms a zone from which ordered phases are excluded, preventing the stabilization of a superconducting phase with d-wave symmetry, i.e., only s-wave pairing is allowed.

Keywords: Magnetism, charge order, superconductivity, extended interactions

Agradecimentos

Agradeço à minha família por serem sempre fonte de inspiração e incentivo. Aos meus irmãos Flávio, Welgatta e Wytila, por todo apoio, suporte e carinho. Agradeço às minhas mães, Lucineide Pereira da Silva e Maria de Jesus Lustosa por nunca medirem esforços para que eu tivesse uma boa educação e condições de seguir meus sonhos. Pelo incondicional apoio em todos os meus projetos e metas. Por me ensinarem, através do seu próprio exemplo, a sempre resilir diante de qualquer revés. Por, mesmo sem terem tido a chance de terminar o ensino básico, sempre terem me ensinado que apenas através da educação eu poderia alcançar meus sonhos. A elas tudo devo e por tudo agradeço.

Agradeço à Amanda Dornela pelos incondicionais apoio e motivação. Por ter estado comigo nos momentos bons e ruins durante esta trajetória. Por ser fonte de inspiração e motivação.

Agradeço a todos os meus amigos do grupo Quantum Matter, muito obrigado por todos os momentos de convivência, suporte e descontração. Em especial, agradeço aos meus leais companheiros: Jorge Basílio, Jéssica Mafra, Paulo Henrique, Felipe Martins, Gabriela Borges e Tiago Viana. Muito obrigado por cada momento de convivência e por estarem presentes nos momentos que mais precisei desde o início da minha jornada. Ao Igor de Souza e Luiza Botelho, da secretaria do PPGF-UFRJ, por todo suporte e gentileza. Agradeço ainda ao professor José Pimentel, por ter desempenhado um papel fundamental na minha formação pessoal e profissional.

Agradeço Sebastião dos Anjos Sousa Júnior pela coorientação e cooperação no desenvolvimento desse projeto. Ao professor Natanael de Carvalho Costa por sempre estar disponível para discussão dos temas relevantes para o projeto e para minha formação.

Agradeço ao professor Raimundo Rocha dos Santos por toda atenção e dedicação em minha orientação. Agradeço ainda por sua constante disponibilidade para discutir física,

tanto nos temas diretamente relacionados ao projeto quanto em temas mais amplos que enriqueceram minha formação. Muito obrigado pela confiança, pelas conversas motivadoras e pelos momentos de inspiração. De modo geral, sua orientação foi fundamental para o meu crescimento acadêmico e profissional. Muito obrigado.

Agradeço às entidades CAPES, CNPq e FAPERJ pelo apoio financeiro no decorrer da realização do trabalho.

"Dotou a mãe-natureza
Com toda filosofia
Fez o Sol e a Lua
O Sol quente e a Lua fria
Para o Sul deu a fartura
Para o Centro, a agricultura
Pro Nordeste, a poesia"

Zé Bezerra

Contents

List of Figures

Introduction

The Hubbard model, proposed by J. Hubbard in 1963 [7], provides one of the simplest ways to study electronic correlations in solids. The model expresses the competition between itinerancy (electron hopping through lattice sites) and localization (due to Coulomb repulsion). Although the model was initially simplified to include only on-site interactions, for mathematical convenience, Hubbard's original formulation already considered the possibility of weaker extended interactions, including nearest-neighbor interactions.

The competition between interactions in itinerant fermionic systems usually gives rise to a multitude of interesting phases [8]. For instance, while magnetic correlations arise from Coulomb repulsion between electrons, coupling with phonon degrees of freedom may induce charge and pairing correlations. From a theoretical perspective, the Extended Hubbard Model (EHM) is one of the simplest models describing emergent magnetic, charge, and superconducting orders in electronic systems. Indeed, while a repulsive on-site interaction, $U > 0$, favors the formation of magnetic moments and their effective coupling, the presence of a repulsive nearest-neighbor interaction, $V > 0$, enhances charge correlations, thus favoring arrangements of doubly occupied sites.

Investigations about the pairing mechanisms of unconventional superconductivity in cuprates suggest that, although in Hubbard's original paper both local and extended interactions are Coulombic ($U, V > 0$), antiferromagnetic fluctuations mediate an effective interaction which is repulsive locally and attractive in nearest-neighbors sites [9, 10]. Indeed, on a half-filled square lattice, an attractive $V < 0$ gives rise to a d-wave superconducting state within a range of values of $U > 0$ [11, 12, 13, 14, 2]; upon doping, this

model is expected to have strong bearings on high-T_c superconductivity in the cuprates [15]. This model has recently been realized in contexts such as the quasi-one-dimensional cuprate $Ba_{2-x}Sr_xCuO_{3+\delta}$ [16], ultracold atoms in optical lattices [17, 18], and in few-dopant quantum dot systems [19].

Phases emerging from competing interactions are often sensitive to the underlying lattice geometry. A simple example is provided by the half-filled Hubbard model (HM) on a kagome lattice with anisotropic hopping: a crossover between kagome and Lieb lattices involves phases such as ferromagnetic insulating, paramagnetic metallic, and Mott insulating [20, 21]. The recent discovery of correlated insulating phases and superconductivity in magic-angle twisted bilayer graphene (TBG) [22, 23] has spawned renewed interest in the study of strongly correlated phenomena on a honeycomb (HC) lattice. Indeed, while electron-electron interactions had previously been invoked to explain the occurrence of a strain-driven semimetal-insulator transition in graphene [24, 25, 26], a recent study pointed towards the potential control of electron-electron interaction in graphene through proximity screening [27]. In addition, some transition-metal dichalcogenides (TMD) with low-dimensional hexagonal-like lattice geometries have been found to exhibit charge-density wave and superconducting phases [28, 29]. A Hubbard-like model for magic-angle TBG has been proposed [30], whose low-energy properties are strongly influenced by electron-electron (e-e) interactions, thus opening the possibility of novel many-body effects [31]. Further, recent matrix Random Phase Approximation (RPA) calculations suggest that the superconducting phase in the magic angle TBG is strongly influenced by local and extended e-e interactions [32]. Finally, we stress that the properties of the HM on the HC lattice are quite different from those on the square lattice: the former displays a semimetallic-antiferromagnetic (SM-AFM) transition at a *finite* value of U [33, 34, 6]; that is, the system goes from a gapless Dirac SM to an insulating magnetically ordered phase with a characteristic Mott gap.

In view of the above, a thorough study of the EHM on a HC lattice is certainly of

interest. We note that the studies so far [5, 35, 36] have been mean-field–based and focused on the first quadrant of the U-V parameter space, namely $U, V > 0$. The picture that emerged at half filling is that in addition to the AFM and SM phases, already present in the HM, a finite $V > 0$ induces the appearance of a charge-density wave (CDW) phase for $V \gtrsim U/3$; upon doping, superconducting phases may be stabilized [35]. One should have in mind that similar half-filling physics occurs in the Hubbard-Holstein model [37], as a result of enhanced charge correlations caused by the electron-phonon coupling. For completeness, we mention that several variants of the EHM on a HC lattice have also predicted the appearance of CDW phases [38, 5, 39, 40], as well as bond-ordered phases [41], and non-trivial topological properties [42].

Our purpose here is to explore the full parameter space of the half-filled EHM on a honeycomb lattice through determinant quantum Monte Carlo (DQMC) simulations. We will focus on the nature of the emerging phases, and on an accurate determination of the different phase boundaries. The extended Hubbard model is described by the Hamiltonian

$$\mathcal{H} = -t \sum_{\langle \mathbf{i},\mathbf{j} \rangle} (c^{\dagger}_{\mathbf{i}\sigma} c_{\mathbf{j}\sigma} + \text{H.c.}) - \mu \sum_{\mathbf{i},\sigma} n_{\mathbf{i},\sigma} + U \sum_{\mathbf{i}} n_{\mathbf{i}\uparrow} n_{\mathbf{i}\downarrow} + V \sum_{\langle \mathbf{i},\mathbf{j} \rangle} n_{\mathbf{i}} n_{\mathbf{j}}, \tag{1}$$

with $c^{\dagger}_{\mathbf{i},\sigma}(c_{\mathbf{i},\sigma})$ being the creation (annihilation) operator for an electron with spin $\sigma(=\uparrow,\downarrow)$ on site $\mathbf{i}$. Here, the sums run over sites of a two-dimensional honeycomb lattice with periodic boundary conditions and $\langle \mathbf{i},\mathbf{j} \rangle$ denotes nearest-neighbor sites only. The first term in Eq. (1) describes fermionic hopping, the second controls the band filling through the chemical potential, μ, with $n_{\mathbf{i},\sigma} \equiv c^{\dagger}_{\mathbf{i},\sigma} c_{\mathbf{i},\sigma}$. The third and fourth terms describe on-site and extended interactions, with strengths U and V, respectively. A schematic representation of the model is depicted in Fig. 1.

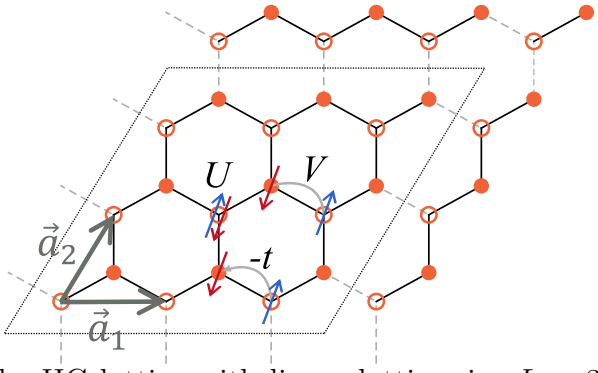

Fig. 1: A portion of the HC lattice with linear lattice size $L = 3$. Sites on each of the two sublattices are represented as (orange) filled and empty circles; primitive vectors are denoted by $\vec{a}_1$ and $\vec{a}_2$. Hoppings $(-t)$ are only allowed between nearest-neighbor (NN) sites, while U and V represent on-site and NN couplings. Periodic boundary conditions are assumed, as indicated by the dashed lines crossing the diamond contour.

The layout of this dissertation is as follows. In Chapter 1 we derive the Hubbard model and present some results for one- and two-dimensional EHM. In Chapter 2 we highlight the determinant quantum Monte Carlo method and some strategies to study phase transitions. Chapter 3 presents the results for the ground-state of the EHM on a honeycomb lattice. Finally, Chapter 4 summarizes our findings.

Chapter 1

The Hubbard Model

1.1 Models for electron correlations in narrow energy bands

We know from quantum mechanics that the physical properties of a many-particle system are fully described by the many-body wave function. Surprisingly, many important properties of condensed matter systems can be satisfactorily explained without accounting for interactions between electrons. However, some properties like magnetism in transition metals or superconductivity in cuprates are strongly dependent on the collective behavior of these particles. The strong correlation between electrons introduces extra complexity, making the theoretical description of these phenomena challenging, especially when accounting for all aspects of a real crystal. Therefore, a simpler model of a solid that accounts for the electronic interaction is very useful for describing strongly correlated phenomena in materials.

In view of the above, electrons in the conduction band of conventional metals are weakly interacting, so that the properties of these metals can be adequately described for a free electron gas model. However, materials such as transition metals and rare-earth have partly filled d and f narrow bands in addition to their conduction bands. Because of this, the correlation phenomena have a greater contribution than the effects of the conduction band in determining the properties of these materials.

In 1963 John Hubbard proposed a model to describe electron correlations in narrow energy bands of $3d-$transition metals [7]. In a d-band the electron charge density is concentrated close to the nuclei of the solid and sparse between the atoms; with this we can think of the electron as being on a particular atom. Indeed, these electrons exhibit characteristics of both the ordinary band model and the atomic model. For example, the large contribution of d-electrons to the specific heat at low temperatures is well explained by a band theory, while the spin-wave phenomena in ferromagnetic metals can be understood with an atomic model. Therefore, a theory of correlation effects in narrow d-bands should primarily focus on achieving a detailed understanding of the balance between band-like and atomic-like behavior. In a few words, the Hubbard model encompasses the interplay between itinerancy and localization of electrons. In what follows, we present a short derivation of the Hubbard Hamiltonian highlighting the main approximations assumed.

Although the real case of interest was $3d$-transition metals, for reasons of mathematical simplicity, the s-band case was considered. The Hamiltonian for an electron in a solid can be written as

$$\mathcal{H} = \sum_{\mathbf{i}} \left[\frac{1}{2m} P_{\mathbf{i}}^2 + V(\mathbf{r_i}) \right] + \frac{1}{2} \sum_{\mathbf{i} \neq \mathbf{j}} \frac{e^2}{|\mathbf{r_i} - \mathbf{r_j}|}, \tag{1.1}$$

where $V(\mathbf{r_i})$ is the potential energy of electron-ion interaction and the last term concerns the electron-electron (e-e) interaction. Let the one-electron term be represented by $h(\mathbf{r_i})$ and $v_{\mathbf{i,j}} \equiv e^2/|\mathbf{r_i} - \mathbf{r_j}|$. Then Eq.(1.1) can be expressed in second quantized form as

$$\mathcal{H} = \sum_{\nu\mu} \langle \nu | h | \mu \rangle c_\nu^\dagger c_\mu + \frac{1}{2} \sum_{\mu\nu\alpha\beta} \langle \mu\nu | v_{\mathbf{i,j}} | \alpha\beta \rangle c_\nu^\dagger c_\mu^\dagger c_\alpha c_\beta, \tag{1.2}$$

with $c_\nu^\dagger (c_\nu)$ being the creation (annihilation) operators for fermions. We now choose a basis of Bloch states, $\psi_{\mathbf{k}}(\mathbf{r})$, to represent Eq.(1.2). In this basis, the Hamiltonian is expressed as

$$\mathcal{H} = \sum_{\mathbf{k}\sigma} \varepsilon_{\mathbf{k}} c_{\mathbf{k}}^\dagger c_{\mathbf{k}} + \frac{1}{2} \sum_{\mathbf{k}_1\mathbf{k}_2\mathbf{k}_1'\mathbf{k}_2'} \sum_{\sigma\sigma'} \langle \mathbf{k}_1\mathbf{k}_2 | \frac{1}{r} | \mathbf{k}_1'\mathbf{k}_2' \rangle c_{\mathbf{k}_1\sigma}^\dagger c_{\mathbf{k}_2\sigma'}^\dagger c_{\mathbf{k}_2'\sigma'} c_{\mathbf{k}_1'\sigma}, \tag{1.3}$$

where $\varepsilon_{\mathbf{k}} = \langle\psi_{\mathbf{k}}|h|\psi_{\mathbf{k}}\rangle$, $\sigma = \{\uparrow,\downarrow\}$ is the spin label and the $\mathbf{k}$ sums run over the first Brillouin zone.

It is convenient to transform the Hamiltonian of Eq.(1.3) by introducing the Wannier functions,

$$\phi(\mathbf{r}-\mathbf{R_i}) = \frac{1}{\sqrt{N}}\sum_{\mathbf{k}}\psi_{\mathbf{k}}(\mathbf{r})e^{-i\mathbf{k}\cdot\mathbf{R_i}}. \tag{1.4}$$

We have the corresponding relation to the creation (annihilation) operators

$$c^{\dagger}_{\mathbf{i}\sigma} = \frac{1}{\sqrt{N}}\sum_{\mathbf{k}}c^{\dagger}_{\mathbf{k}\sigma}e^{-i\mathbf{k}\cdot\mathbf{R_i}}, \qquad c_{\mathbf{i}\sigma} = \frac{1}{\sqrt{N}}\sum_{\mathbf{k}}c_{\mathbf{k}\sigma}e^{i\mathbf{k}\cdot\mathbf{R_i}}. \tag{1.5}$$

With this, the transformed Hamiltonian reads

$$\mathcal{H} = \sum_{\mathbf{ij}}\sum_{\sigma}T_{\mathbf{ij}}c^{\dagger}_{\mathbf{i}\sigma}c_{\mathbf{j}\sigma} + \frac{1}{2}\sum_{\mathbf{ijlm}}\sum_{\sigma\sigma'}\langle\mathbf{ij}|\frac{1}{r}|\mathbf{lm}\rangle c^{\dagger}_{\mathbf{i}\sigma}c^{\dagger}_{\mathbf{j}\sigma'}c_{\mathbf{m}\sigma'}c_{\mathbf{l}\sigma}, \tag{1.6}$$

where,

$$T_{\mathbf{ij}} = \frac{1}{N}\sum_{\mathbf{k}}\varepsilon_{\mathbf{k}}e^{i\mathbf{k}\cdot(\mathbf{R_i}-\mathbf{R_j})} \tag{1.7}$$

and

$$\langle\mathbf{ij}|\frac{1}{r}|\mathbf{lm}\rangle = e^2\int\frac{\phi^*(\mathbf{r}-\mathbf{R_i})\phi^*(\mathbf{r}-\mathbf{R_j})\phi(\mathbf{r}-\mathbf{R_l})\phi(\mathbf{r}-\mathbf{R_m})}{|\mathbf{r}'-\mathbf{r}|}d\mathbf{r}d\mathbf{r}'. \tag{1.8}$$

With the Hamiltonian expressed in the form of Eq. (1.6), the main approximation can be made. Since one is considering a narrow band, the Wannier functions will closely resemble atomic s-orbitals. Furthermore, if we assume a small bandwidth, these s-orbitals must form an atomic shell with a radius smaller than the interatomic distance. With this, we can see through Eq.(1.8) that the on-site interaction, namely $U \equiv \langle\mathbf{ii}|1/r|\mathbf{ii}\rangle$, will be greater in magnitude than other integrals. This suggests that, in a *first* approximation, all other possible integrals can be neglected. With this approximation, Eq.(1.6) turns into the Hubbard model Hamiltonian

$$\mathcal{H} = \sum_{\mathbf{ij}}\sum_{\sigma}T_{\mathbf{ij}}c^{\dagger}_{\mathbf{i}\sigma}c_{\mathbf{j}\sigma} + \frac{U}{2}\sum_{\mathbf{i}}n_{\mathbf{i}\uparrow}n_{\mathbf{i}\downarrow}, \tag{1.9}$$

where, $n_{\mathbf{i}\sigma} = c^{\dagger}_{\mathbf{i}\sigma}c_{\mathbf{i}\sigma}$ is the number operator.

The largest term of Eq.(1.8) neglected in the Hubbard model represents the nearest-neighbor interactions, $V \equiv \langle \mathbf{ij}|1/r|\mathbf{ij}\rangle$; this term allows for accounting the effects of non-local electronic correlations. This improvement in the first approximation gives rise to the extended Hubbard model, whose Hamiltonian reads

$$\mathcal{H} = \sum_{\mathbf{ij}} \sum_{\sigma} T_{\mathbf{ij}} c^{\dagger}_{\mathbf{i}\sigma} c_{\mathbf{j}\sigma} + \frac{U}{2} \sum_{\mathbf{i}} n_{\mathbf{i}\uparrow} n_{\mathbf{i}\downarrow} + \frac{V}{2} \sum_{\mathbf{ij}} \sum_{\sigma} n_{\mathbf{i}\sigma} n_{\mathbf{j}\sigma}. \tag{1.10}$$

For the sake of comparison, in $3d$-transition metals the ratio between the order of magnitude of local and extended interactions is $V/U = 0.3$, which suggests that the inclusion of the extended interactions term is quite appreciable.

Although Hubbard models were initially proposed for studying $3d$-transition metals, over the years, they have been employed to describe a wide range of phenomena in condensed matter physics. Examples include high-temperature superconductivity in cuprates [9], the emergence of various strongly correlated phases in twisted bilayer graphene systems [30, 31], and in the context of topological phase transitions [43].

1.2 Attractive electron-electron interactions

In the previous section we presented the motivations and formulation of the on-site and extended Hubbard models. As discussed above, initially both local and nearest-neighbor electron-electron interactions on the Hamiltonian are Coulombic (repulsive), *i.e.,* $U, V > 0$ in Eq.(1.10). However, alternative versions of both models with effective local and/or nearest-neighbor attraction have been largely employed to explore correlation effects [44, 9, 10, 45].

In the context of narrow energy bands, two electrons can effectively interact with each other attractively, leading to the formation of local pairs. The simplest mechanism for the formation of these pairs comes from the electron-lattice interaction, which favors the formation of polarons. Two polarons interact attractively through the induced deformation of the lattice and form a local pair if this attraction overcomes the Coulomb repulsion.

This effective attraction can lead to phases such as superconductivity and charge-density wave, found in a vast list of materials [44]. This mechanism is well featured setting an attractive on-site interaction ($U < 0$) on the extended Hubbard Hamiltonian. Furthermore, the attractive Hubbard model was also employed to study phenomena such as the BCS-BEC crossover [45] and mechanisms to increase the critical temperature of the superconducting phase [46, 47].

Cuprates are well-known materials for exhibiting superconductivity with higher critical temperatures compared to conventional superconductors [48]. Unlike BCS superconductors [49], these materials exhibit strong e-e interactions and an unconventional d-wave pairing symmetry. Another common feature of cuprates is the antiferromagnetic (AFM) order in the undoped regime, with the superconducting state emerging when the system is doped with holes. This suggests that spin fluctuations may play an important role in the formation of pairs. However, the exact mechanism behind the pairing remains unknown. In this context, the Hubbard model and its variants provide the simplest way to describe several properties of these materials, thus making it reasonable to examine the pairing interactions within these models. In this case the pairing interaction is given by the irreducible particle-particle four-point vertex [10]. As discussed in Ref.[10], the AFM spin fluctuations lead to a spatially non-local pairing interaction, characterized by on-site repulsion ($U > 0$) and nearest-neighbor attraction ($V < 0$).

1.3 Extended Hubbard model

1.3.1 Extended Hubbard model at half-filling

The extended Hubbard model (EHM) is a straightforward approach to describe the effects of competition between local and non-local electronic correlations. While the Coulomb on-site repulsion favors the formation and coupling of magnetic moments, the nearest-neighbor repulsion increases charge correlations, leading to charge ordered phases. Furthermore, if one allows for effective attractive interactions, superconducting and phase

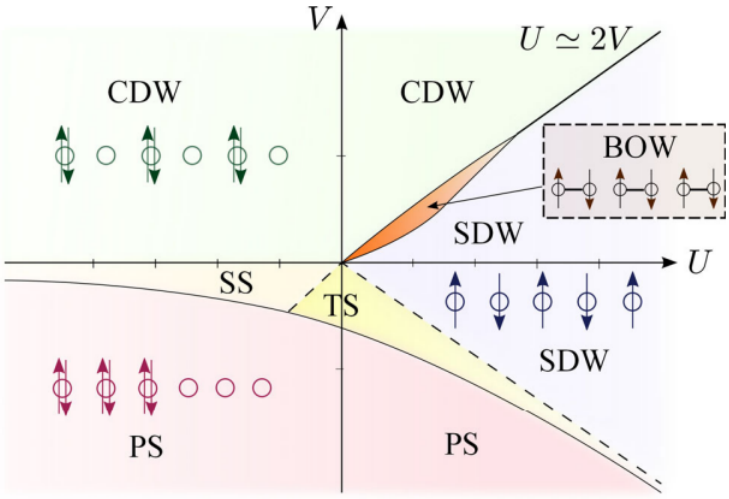

Fig. 1.1: Ground state phase diagram for the half-filled extended Hubbard model in one dimension. Figure extracted from Ref.[1]

separated states may be stabilized. In view of this, the EHM is expected to exhibit a rich phase diagram, especially when considering positive and negative values for U and V. Therefore, it is important to investigate the EHM phase diagrams and how it is influenced by different electronic structures and band fillings.

The ground state phase diagram for the half-filled EHM in one dimension is already known [50], as summarized in Fig 1.1. On-site repulsion favors a spin-density wave phase, while the first-neighbor repulsion induces a charge-density wave; the boundary between these phases is near the $U = 2V$ line. The system also exhibits a bond-ordered wave (BOW) phase; see Fig 1.1. For $V < 0$ the superconducting (SC) phases appear for both repulsive or attractive on-site interaction. Furthermore, strong nearest-neighbor attraction induces a phase separated (PS) phase. This state is characterized by a superposition of empty and fully doubly occupied system; see Fig.1.1.

It is interesting to analyze what happens when $t = 0$, namely the atomic limit. For a bipartite lattice, the CDW and AFM states, depicted for a square lattice in Fig.1.2, have energies

$$E_{afm} = \frac{z}{2}NV \qquad \text{and} \qquad E_{cdw} = \frac{1}{2}NU, \tag{1.11}$$

where N is the number of sites and z is the coordination number; $z = 4$ for the square

lattice. The boundary between these phases is obtained by equating the energies, $E_{afm} = E_{cdw}$. We then obtain the strong coupling boundary line $V = U/4$, for the square lattice. Interestingly, this line also defines the region within which the complex field transformation of DQMC remains valid. Further details on this can be found in Appendix A.

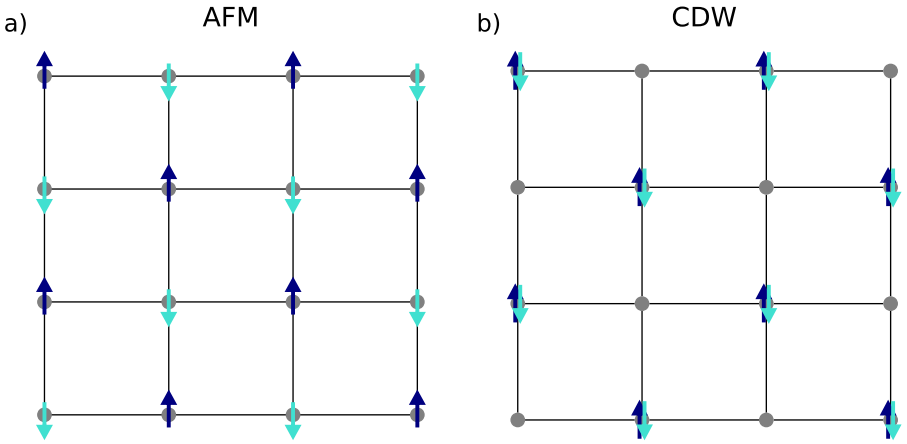

Fig. 1.2: Square lattice with (a) antiferromagnetic and (b) charge-density wave arrangements.

Beyond the atomic limit, an accurate ground state phase diagram was recently proposed for a half-filled square lattice [2]; see Fig 1.3. Similarly to the one-dimensional case, here on-site repulsion induces an antiferromagnetic phase (AFM), while nearest-neighbor repulsion favors the CDW state. For the $V < 0$ half-plane, s- and d-wave superconducting phases emerge. We notice that the s-wave state only appears in the $U < 0$ region, while the d-wave phase is stabilized in both $U < 0$ and $U > 0$ sectors. Finally, there is a PS state for the range of U considered and sufficiently strong nearest-neighbor attraction.

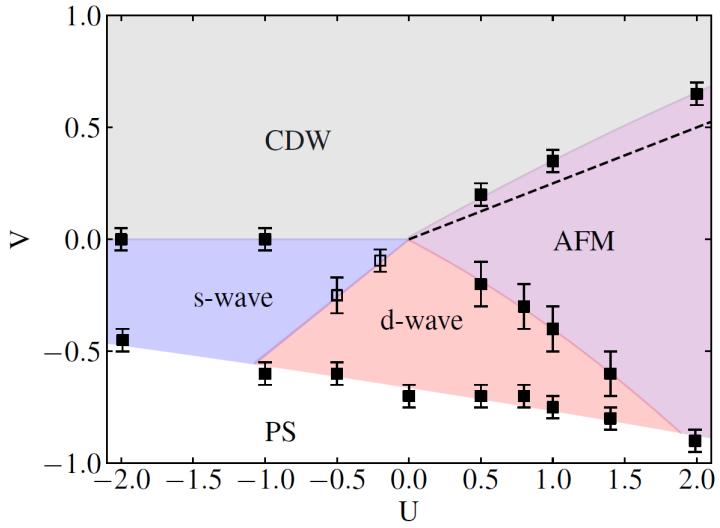

Fig. 1.3: Ground state phase diagram for the half-filled extended Hubbard model on a square lattice. The dashed line represents the strong coupling boundary line. Figure extracted from Ref.[2]

1.3.2 Extended Hubbard model at quarter-filling

Although the previous analysis provides valuable insights about the competition of local and extended interactions, one expects that away from half-filling new phenomena may arise. As mentioned before, for several cuprates, which are antiferromagnetic at half-filling, the superconducting phase only emerges when the system is doped with holes. In this way, the analysis of the EHM for different fillings is certainly of interest. In what follows, some properties of the quarter-filled ($n = 0.5$) EHM are presented.

For the one-dimensional model, the ground state phase diagram has been investigated using renormalization group (RG) techniques, for $U, V > 0$ [51, 3]. The diagram in Fig.1.4 is quite different from the half-filled case, the main differences being the absence of the SDW phase and the emergence of metallic and superconducting phases; a SC phase is predicted to emerge in the region $V \gg U$. Another difference observed is the substantial increase in the values of U and V necessary to stabilize the CDW/insulator phase (cyan area).

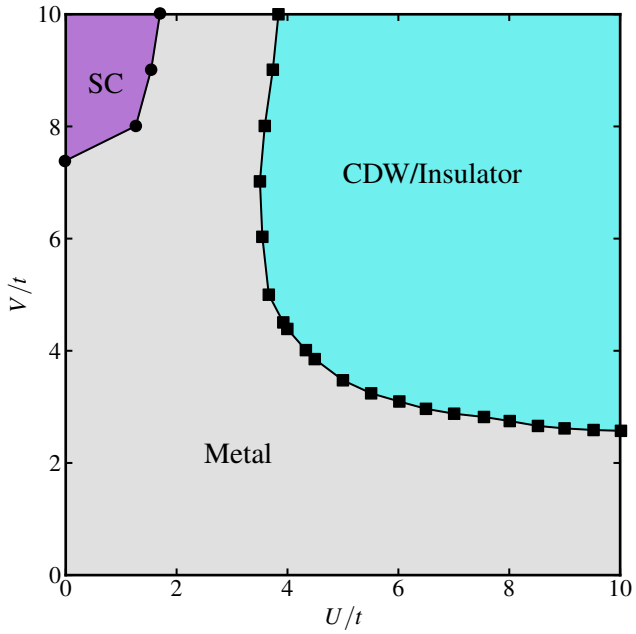

Fig. 1.4: Ground state phase diagram for the one-dimensional quarter-filled extended Hubbard model. Figure adapted from Ref.[3]

Inspired by the similarities between the one- and two-dimensional cases at half-filling, one may expect the emergence of corresponding phases for the square lattice at $n = 0.5$. As an example, the lack of a perfectly nested Fermi surface at this band filling may lead to the emergence of a metallic phase.

The ground state of the EHM on a quarter-filled square lattice was recently investigated through Lanczos exact diagonalization (LED) and DQMC [4]. Results for the charge and s-wave pairing structure factors provided invaluable insights about the phase diagram. Figure 1.5 (a) displays a contour plot of the charge structure factor, S_{cdw}, as a function of U and V. For strong on-site and first-neighbor interactions, the increased S_{cdw} region suggests the stabilization of the CDW phase. Additionally, DQMC results for critical points, obtained by tracking the maximum derivative of S_{cdw}, are depicted in magenta diamonds. Figure 1.5 (b) shows an analogous plot for the pairing structure factor, P_s. For weak U and strong V an increased P_s region is formed, indicating that a superconducting phase could emerge. Blue diamonds represent DQMC results for critical

points obtained through the analysis of the average sign of fermionic determinants, $\langle s \rangle$; more on this in Sec. 2.4. We note that the phase boundaries obtained through $\langle s \rangle$ do not quite agree with the boundaries obtained from the correlation functions.

Despite these promising results, the confirmation of these phases requires a thorough finite size scaling (FSS) analysis. However, this demands additional calculations for larger systems, which is currently intractable with LED due to computational limitations; DQMC simulations are also hindered by a severe minus-sign problem.

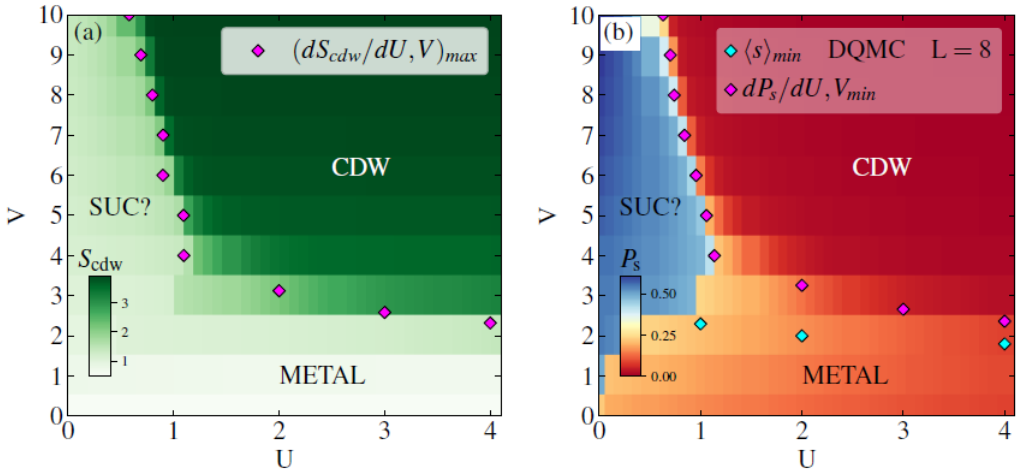

Fig. 1.5: Lanczos exact diagonalization (contour plot) and DQMC (markers) results for the (a) charge and (b) pairing structure factors. Figure adapted from Ref.[4]

The above discussion illustrates the richness of phenomena displayed by the EHM in general. In particular, investigation of the extended Hubbard model in different geometries should lead to unexpected behaviors. For instance, the lack of perfect nesting and of a van Hove singularity on a half-filled HC lattice may drastically influence the phase diagram. With this in mind, here we use DQMC to obtain the phase diagram of the EHM on a HC lattice at half-filling.

Chapter 2

Determinant Quantum Monte Carlo

The Determinant Quantum Monte Carlo (DQMC) method [52, 53, 54, 55, 56, 57, 58] is a powerful tool for studying both zero and finite temperature properties of several strongly correlated system models. In this chapter, we present a discussion focused on the main aspects of the method applied to fermionic Hamiltonians. In Sec. 2.1 we present a detailed discussion about the formulation of the method, focusing on the key steps, applied to the Hubbard model. In Sec. 2.2 we adapt these ideas to the extended Hubbard model. In Sec. 2.3 we discuss correlation ratios and how they can be used to estimate quantum critical points. Finally, in Sec. 2.4 we discuss the origin and consequences of the "minus-sign problem", as well as the recent observation that this problem can also provide information about phase transitions.

2.1 On-site interaction: the Hubbard model

For simplicity we start our discussion by considering the Hubbard model,

$$\mathcal{H} = \mathcal{H}_{\mathcal{K}} + \mathcal{H}_{\mathcal{I}} = -t \sum_{\langle \mathbf{i},\mathbf{j} \rangle} (c^{\dagger}_{\mathbf{i}\sigma} c_{\mathbf{j}\sigma} + \text{H.c.}) - \mu \sum_{\mathbf{i}\sigma} n_{\mathbf{i},\sigma} + U \sum_{\mathbf{i}} n_{\mathbf{i}\uparrow} n_{\mathbf{i}\downarrow}. \tag{2.1}$$

In order to calculate the partition function we need to compute the Boltzmann operator, $e^{-\beta(\mathcal{H}_{\mathcal{K}}+\mathcal{H}_{I})}$. Since the kinetic and interaction terms do not commute, we perform a Suzuki-

Trotter decomposition to separate the operator as a product of exponentials

$$e^{-\beta(\mathcal{H}_{\mathcal{K}}+\mathcal{H}_{I})} \approx \left(e^{-\Delta\tau\mathcal{H}_{\mathcal{K}}}e^{-\Delta\tau\mathcal{H}_{\mathcal{I}}}\right)^{N_\tau} + \mathcal{O}\left(\Delta\tau^2\right), \tag{2.2}$$

where $\Delta\tau = \beta/N_\tau$.

The Suzuki-Trotter decomposition introduces a new dimension to the system, the imaginary time axis. Notice that the inverse temperature, β, is divided into N_τ discrete intervals (time-slices). Furthermore, such decomposition leads to an error of $\mathcal{O}\left(\Delta\tau^2\right)$, and the choice $\Delta\tau = 0.1$ typically leads to errors smaller than statistical ones, allowing us to neglect Trotter errors.

While the kinetic term can be easily diagonalized by using a spinor basis and then performing a similarity transformation, the same is not valid for the interaction (quartic) term. Therefore, this term needs to be carefully treated in a many-body context. The quartic term in the exponential of the interaction part is expressed in a quadratic form by applying a discrete Hubbard-Stratonovich (HS) transformation [53, 11],

$$e^{-\Delta\tau U n_{\mathbf{i}\uparrow} n_{\mathbf{i}\downarrow}} = \begin{cases} \frac{1}{2}\sum_{s_\nu=\pm1} e^{\left[\alpha s_\nu (n_{\mathbf{i}\uparrow}-n_{\mathbf{i}\downarrow}) - \frac{\Delta\tau U}{2}(n_{\mathbf{i}\uparrow}+n_{\mathbf{i}\downarrow})\right]} & \text{for } U>0 \\ \\ \frac{1}{2}\sum_{s_\nu=\pm1} e^{\left[\alpha s_\nu (n_{\mathbf{i}\uparrow}+n_{\mathbf{i}\downarrow}-1) - \frac{\Delta\tau U}{2}(n_{\mathbf{i}\uparrow}+n_{\mathbf{i}\downarrow})\right]} & \text{for } U<0 \end{cases} \tag{2.3}$$

where $\cosh\alpha = e^{\Delta\tau|U|2}$.

The HS transformation breaks the interaction term for each time-slice in a sum of non-interacting terms, introducing Ising fields, $s_\nu = \pm 1$, and leading to a convenient form in which there are only bilinear terms in the exponential. Notice that this approach allows us to map a d-dimensional quantum system into a $d+1$ classical system. Working on a honeycomb lattice with periodic boundary conditions with N sites, the HS transformation produces $N \times N_\tau$ Ising fields. As an example, the partition function for the repulsive case ($U > 0$) becomes

$$\mathcal{Z} = \left(\frac{1}{2}\right)^{NN_\tau} \operatorname*{\mathbf{Tr}}_{\{s\}} \operatorname*{\mathbf{Tr}}_{\{n\}} \prod_{\ell=N_\tau}^{1} \prod_{\sigma=\uparrow,\downarrow} e^{-\Delta\tau\sum_{\mathbf{i},\mathbf{j}} c^\dagger_{\mathbf{i}\sigma} K_{ij} c_{\mathbf{j}\sigma}} e^{-\Delta\tau\sum_{\mathbf{i}} c^\dagger_{\mathbf{i}\sigma} V_i^\sigma(\ell) c_{\mathbf{i}\sigma}}, \tag{2.4}$$

where $\mathbf{Tr}_{\{s\}}$ and $\mathbf{Tr}_{\{n\}}$ are the traces over the HS fields and the fermionic degrees of freedom, respectively, and ℓ labels the time-slices. The HS fields acquire two indices labeling its space-time position $s_\nu \to s_\nu(\mathbf{i}, l)$. Finally, $K_{i,j}$ are the elements of the hopping matrix, $\widehat{\mathrm{K}}$, and

$$V_i^\sigma(\ell) = \frac{1}{\Delta\tau}\alpha\sigma s_\nu(\mathbf{i},\ell) + \left(\mu - \frac{U}{2}\right) \tag{2.5}$$

are the elements of a diagonal matrix $\widehat{\mathrm{V}}^\sigma(\ell)$.

With this bilinear form of the exponential, the fermionic degrees of freedom can be traced out of Eq. (2.4),

$$\mathcal{Z} = \left(\frac{1}{2}\right)^{NN_\tau} \underset{\{s\}}{\mathbf{Tr}} \det \mathrm{O}^\uparrow(\{s\}) \cdot \det \mathrm{O}^\downarrow(\{s\}), \tag{2.6}$$

with

$$\mathrm{O}^\sigma(\{s\}) = \mathbb{I} + \mathrm{B}^\sigma_{N_\tau}\mathrm{B}^\sigma_{N_\tau-1}\cdots\mathrm{B}^\sigma_1, \tag{2.7}$$

and

$$\mathrm{B}^\sigma_\ell \equiv e^{-\Delta\tau\widehat{\mathrm{K}}}e^{-\Delta\tau\widehat{\mathrm{V}}^\sigma(\ell)}. \tag{2.8}$$

We can also compute the single-particle equal-time Green's function

$$G^\sigma(\tau,\tau) = \mathbb{I} - \left[\mathbb{I} + \mathrm{B}^\sigma(\tau,0)\mathrm{B}^\sigma(\beta,0)\right]^{-1}. \tag{2.9}$$

The partition function is then expressed as a trace over HS fields of a product of fermionic determinants. If this quantity were positive, we could use it as a statistical weight to perform importance sampling. However, the product of fermionic determinants is not a positive-definite quantity, giving rise to the minus-sign problem, which we will discuss in Sec. 2.4.

Since the number of auxiliary fields grows with 2^{NN_τ} we have to perform Monte Carlo importance sampling over $\{s\}$ to calculate the partition function. The sampling over the HS fields consists of sweeps over the sites trying to make a flip, $s_\nu \to s'_\nu$, on a generic site, $\mathbf{i}$, of a generic time slice, ℓ. Let $\{s\}$ and $\{s'\}$ be the HS fields configurations, we then

write the ratio of statistical weights as

$$r' = \frac{\det \mathrm{O}^{\uparrow}_{\{s'\}} \cdot \det \mathrm{O}^{\downarrow}_{\{s'\}}}{\det \mathrm{O}^{\uparrow}_{\{s\}} \cdot \det \mathrm{O}^{\downarrow}_{\{s\}}}. \tag{2.10}$$

The decision of whether a proposed change is accepted is made using the Metropolis or heat-bath algorithms [56, 59, 60].

Another advantage of this approach is that all average values are expressed in terms of Green's functions. The standard definition of the matrix elements of the single-particle equal-time Green's function is

$$G^{\sigma}_{\mathbf{ij}} \equiv \langle c_{\mathbf{i}\sigma} c^{\dagger}_{\mathbf{j}\sigma} \rangle = \delta_{\mathbf{ji}} - \langle c^{\dagger}_{\mathbf{j}\sigma} c_{\mathbf{i}\sigma} \rangle. \tag{2.11}$$

As an example, the occupation is given by

$$n = \frac{1}{NN_{\tau}} \sum_{\mathbf{i},\ell} \sum_{\sigma} \langle c^{\dagger}_{\mathbf{i}\sigma}(\ell) c_{\mathbf{i}\sigma}(\ell) \rangle = \frac{1}{NN_{\tau}} \sum_{\mathbf{i},\ell} \sum_{\sigma} \langle 1 - G^{\sigma}_{\mathbf{ii}}(\ell) \rangle_{\{s\}}, \tag{2.12}$$

with the average in the second equality being performed over the HS fields. In this approach the fermions only couple with the HS fields, so that Wick's theorem [61] is still valid for a fixed HS fields configuration, and then we can use it to express any two-particle Green's function in terms of the single-particle Green's function,

$$\langle c^{\dagger}_{i1} c_{i2} c^{\dagger}_{i3} c_{i4} \rangle = \langle c^{\dagger}_{i1} c_{i2} \rangle \langle c^{\dagger}_{i3} c_{i4} \rangle + \langle c^{\dagger}_{i1} c_{i4} \rangle \langle c^{\dagger}_{i2} c_{i3} \rangle; \tag{2.13}$$

with this, we are able to calculate several equal-time correlation functions.

2.2 Nearest neighbor interaction: the extended Hubbard model

The previous section presented an overview of the DQMC applied to on-site interactions. Now we extend these ideas to the Extended Hubbard Model (EHM), which additionally considers nearest-neighbor interactions with strength V. The EHM Hamiltonian reads

$$\mathcal{H} = -t \sum_{\langle \mathbf{i},\mathbf{j} \rangle} (c^{\dagger}_{\mathbf{i}\sigma} c_{\mathbf{j}\sigma} + \mathrm{H.c.}) - \mu \sum_{\mathbf{i},\sigma} n_{\mathbf{i},\sigma} + U \sum_{\mathbf{i}} n_{\mathbf{i}\uparrow} n_{\mathbf{i}\downarrow} + V \sum_{\langle \mathbf{i},\mathbf{j} \rangle} n_{\mathbf{i}} n_{\mathbf{j}}, \tag{2.14}$$

The first difference relative to the on-site case comes from the Hubbard-Stratonovich transformation, specifically in the number of HS fields. The on-site term has only one product of density operators, then we have to perform just one HS transformation, Eq.(2.3), introducing one auxiliary field, $s_0(\mathbf{i}, \ell)$, for each site $\mathbf{i}$ and time-slice ℓ. Since the extended interaction term is expanded as

$$V \sum_{\langle \mathbf{i},\mathbf{j} \rangle} n_{\mathbf{i}} n_{\mathbf{j}} = V \sum_{\langle \mathbf{i},\mathbf{j} \rangle} (n_{\mathbf{i}\uparrow} n_{\mathbf{j}\uparrow} + n_{\mathbf{i}\uparrow} n_{\mathbf{j}\downarrow} + n_{\mathbf{i}\downarrow} n_{\mathbf{j}\uparrow} + n_{\mathbf{i}\downarrow} n_{\mathbf{j}\uparrow}), \tag{2.15}$$

we have to perform one HS transformation for each product of density operators, which, in turn, introduces four additional auxiliary fields for each bond connecting nearest-neighbor sites $\mathbf{i}$ and $\mathbf{j}$, namely $s_1(\mathbf{i}, \mathbf{j}, \ell)$, $s_2(\mathbf{i}, \mathbf{j}, \ell)$, $s_3(\mathbf{i}, \mathbf{j}, \ell)$, $s_4(\mathbf{i}, \mathbf{j}, \ell)$. A schematic representation of the HS fields on a honeycomb lattice is depicted in Fig. 2.1

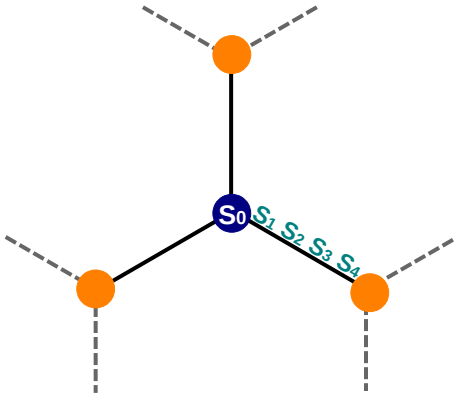

Fig. 2.1: Portion of a honeycomb lattice with the HS fields for the local (s_0) and nearest-neighbor (s_ν) interactions.

For a honeycomb lattice with periodic boundary conditions and $N = 2(L \times L)$ sites, with L being the linear size of the lattice, we have $3 \times L^2$ bonds. Thus the extended interaction term produces $12 \times L^2 \times N_\tau$ auxiliary fields. The on-site term produces $2 \times L^2 \times N_\tau$ additional auxiliary fields. Then the partition function of the system is written as

$$\mathcal{Z} = \left(\frac{1}{2}\right)^{14L^2 N_\tau} \mathop{\mathbf{Tr}}_{\{s_\nu\}} \det \mathrm{O}^{\uparrow}(\{s_0, s_1, s_2, s_3, s_4\}) \cdot \det \mathrm{O}^{\downarrow}(\{s_0, s_1, s_2, s_3, s_4\}), \tag{2.16}$$

with

$$\mathrm{O}^{\sigma}(\{s_0, s_1, s_2, s_3, s_4\}) = \mathbb{I} + \mathrm{B}^{\sigma}_{N_\tau}\mathrm{B}^{\sigma}_{N_\tau-1}\cdots\mathrm{B}^{\sigma}_{1}, \tag{2.17}$$

and

$$\mathrm{B}^{\sigma}_{\ell} \equiv e^{-\Delta\tau\widehat{\mathrm{K}}}e^{-\Delta\tau\widehat{\mathrm{U}}^{\sigma}(\ell)}e^{-\Delta\tau\widehat{\mathrm{V}}^{\sigma}(\ell)}. \tag{2.18}$$

Finally, we can also compute the single-particle equal-time Green's function

$$G^{\sigma}(\tau,\tau) = \mathbb{I} - \left[\mathbb{I} + \mathrm{B}^{\sigma}(\tau,0)\mathrm{B}^{\sigma}(\beta,0)\right]^{-1}, \tag{2.19}$$

through which we calculate all relevant physical quantities. As in the on-site case, since we have $2^{14L^2N_\tau}$ auxiliary fields, we perform Monte Carlo importance sampling over $\{s_0, s_1, s_2, s_3, s_4\}$, to analyze the ground state properties of the extended Hubbard model on a honeycomb lattice.

In order to investigate the occurrence of different ordered phases, we examine the staggered charge structure factor,

$$S_{\mathrm{cdw}}(\mathbf{q}) = \frac{1}{N}\sum_{\mathbf{r_i},\mathbf{r_j}} e^{-i\mathbf{q}\cdot(\mathbf{r_i}-\mathbf{r_j})}\langle(n_{A,\mathbf{r_i}}-n_{B,\mathbf{r_i}})(n_{A,\mathbf{r_j}}-n_{B,\mathbf{r_j}})\rangle, \tag{2.20}$$

and the antiferromagnetic structure factor,

$$S_{\mathrm{afm}}(\mathbf{q}) = \frac{1}{N}\sum_{\mathbf{r_i},\mathbf{r_j}} e^{-i\mathbf{q}\cdot(\mathbf{r_i}-\mathbf{r_j})}\langle(S^z_{A,\mathbf{r_i}}-S^z_{B,\mathbf{r_i}})(S^z_{A,\mathbf{r_j}}-S^z_{B,\mathbf{r_j}})\rangle, \tag{2.21}$$

where $n_{\lambda,\mathbf{r_i}} = n_{\lambda,\mathbf{r_i}\uparrow} + n_{\lambda,\mathbf{r_i}\downarrow}$, and $S^z_{\lambda,\mathbf{r_i}} = n_{\lambda,\mathbf{r_i}\uparrow} - n_{\lambda,\mathbf{r_i}\downarrow}$. Here $\lambda = A, B$ labels the sublattices, while $\mathbf{r_i}$ is the unit cell position of a given site $\mathbf{i}$. We also examine superconducting correlations through the pairing structure factor,

$$S^{\beta}_{\mathrm{sc}}(\mathbf{q}) = \frac{1}{N}\sum_{\mathbf{i},\mathbf{j}} e^{-i\mathbf{q}\cdot(\mathbf{r_i}-\mathbf{r_j})}\langle(\Delta^{\beta}_{A,\mathbf{i}} + \Delta^{\beta}_{B,\mathbf{i}})(\Delta^{\beta\dagger}_{A,\mathbf{j}} + \Delta^{\beta\dagger}_{B,\mathbf{j}})\rangle, \tag{2.22}$$

with

$$\Delta^{\beta}_{\lambda,\mathbf{i}} = \sum_{\mathbf{a}} f^{\beta}(\mathbf{a})c_{\mathbf{i}\downarrow}c_{\mathbf{i}+\mathbf{a}\uparrow}, \tag{2.23}$$

where $f^{\beta}(\mathbf{a})$ is the form factor for a given pair-wave symmetry, $\beta = s, s^*, d, d^*, p, p^*, f$ [62, 63, 64].

It is important to stress that when we use the present approach to the EHM, even with particle-hole symmetry, it suffers from the infamous minus-sign problem. We resort to two strategies to ensure our analysis when the problem becomes severe. The first is the use of the average sign of fermionic determinants as a locator of quantum critical points, which we will discuss in Sec. 2.4. Alternatively, we use a second approach, which resorts to a complex HS fields (CHSF) transformation, which allows for sign-free calculations. We present the details of this approach in Appendix A, where we show that it is only applicable for $|V| \leq |U|/z$, where z is the coordination number.

2.3 Correlation ratios

Phase boundaries and associated critical exponents may also be determined through the correlation ratio [65, 66, 67, 68, 69],

$$R_\gamma(L,V) = 1 - \frac{S_\gamma(\mathbf{q}+\delta\mathbf{q})}{S_\gamma(\mathbf{q})}, \tag{2.24}$$

where $\mathbf{q} = (0,0)$, $\delta\mathbf{q}$ is chosen as its nearest- or next-nearest–neighbor reciprocal wave vector, and γ denotes "cdw", "afm" or "sc". On the HC reciprocal lattice, the two nonequivalent nearest neighbors of $\mathbf{q} = (0,0)$ are $\delta_{\mathbf{q}}^{(0,1)} = \widehat{\mathbf{b}}_2/L$ and $\delta_{\mathbf{q}}^{(1,1)} = (\widehat{\mathbf{b}}_1 + \widehat{\mathbf{b}}_2)/L$, where $\widehat{\mathbf{b}}_1$ and $\widehat{\mathbf{b}}_2$ are the reciprocal lattice basis vectors, as depicted in Fig. 2.2.

Near the critical point and for sufficiently large system sizes, the correlation ratio obeys a finite-size scaling (FSS) form [70, 71, 72], which, by virtue of being a dimensionless quantity, may be written as

$$R_\gamma(L,V) = \mathcal{F}[(V - V_c)\, L^{1/\nu}], \tag{2.25}$$

where $\mathcal{F}$ is an unknown function of its argument and ν is the correlation length critical exponent. Therefore, $\mathcal{F}(0)$ is a constant independent of L at the critical point, so that plots of $R_\gamma(V)$ for different L's should cross at V_c, thus providing estimates for the critical point; these, in turn, should converge towards the exact value as $L \to \infty$.

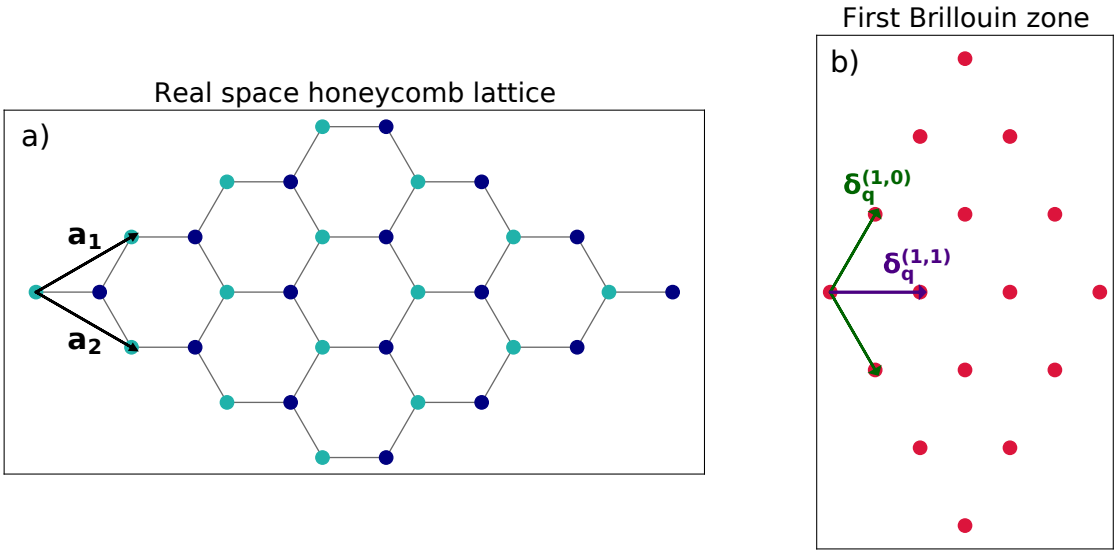

Fig. 2.2: (a) A portion of the real space honeycomb lattice. Sites on each of the two sublattices are represented as turquoise and blue circles; primitive vectors are denoted by $\mathbf{a}_1$ and $\mathbf{a}_2$. (b) First Brillouin zone of the honeycomb lattice. Nearest-neighbor vectors of $\mathbf{q} = (0, 0)$, namely $\delta_{\mathbf{q}}^{(1,0)}$ and $\delta_{\mathbf{q}}^{(1,1)}$, are represented by green and indigo arrows.

And, finally, we take $\beta = L$ to project the ground state, assuming Lorentz invariance at the QCP's [34, 6, 73]. In the next chapter, we use the correlation ratios associated with various ordered phases to locate the boundaries of different quantum phase transitions.

2.4 The minus-sign problem

As discussed before, the statistical weight of each HS configuration is expressed as a product of fermionic determinants

$$W_{\{s\}} = \mathrm{detO}^{\uparrow}(\{s\}) \cdot \mathrm{detO}^{\downarrow}(\{s\}). \tag{2.26}$$

This product is not a positive definite quantity, unless a symmetry exists that ensures a positive value of $W_{\{s\}}$. An example of such a case is the repulsive Hubbard model at half-filling. It can be shown [56] that applying a particle-hole symmetry,

$$c_{\mathbf{i},\sigma}^{\dagger} \rightarrow d_{\mathbf{i}\sigma} = (-1)^{\mathbf{i}} c_{\mathbf{i}\sigma}^{\dagger}, \qquad c_{\mathbf{i}\sigma} \rightarrow d_{\mathbf{i}\sigma}^{\dagger} = (-1)^{\mathbf{i}} c_{\mathbf{i}\sigma}, \tag{2.27}$$

and evaluating the fermionic determinant at half-filling, $\mu = U/2$, we get

$$\mathrm{detO}^{\uparrow}(\{s\}) = e^{-\alpha \sum_{\mathbf{i},\ell} s_{\nu}(\mathbf{i},\ell)} \mathrm{detO}^{\downarrow}(\{s\}). \tag{2.28}$$

Therefore,

$$W_{\{s\}} = \mathrm{detO}^{\uparrow}(\{s\}) \cdot \mathrm{detO}^{\downarrow}(\{s\}) > 0, \quad \text{for} \quad n = 1, U \geq 0, \tag{2.29}$$

and can be used as a statistical weight.

However, in most cases $W_{\{s\}}$ becomes negative for some configurations. To illustrate how to deal with this, let us rewrite the partition function as a sum over configurations $c \equiv \{s\}$,

$$\mathcal{Z} = \left(\frac{1}{2}\right)^{NN_{\tau}} \mathop{\mathbf{Tr}}_{\{s\}} \mathrm{detO}^{\uparrow}(\{s\}) \cdot \mathrm{detO}^{\downarrow}(\{s\}) = \sum_{c} W(c). \tag{2.30}$$

If we define $W(c) \equiv h(c)|W(c)|$, with $h(c) = \pm 1$, we can rewrite the average value of any quantity A as follows

$$\begin{aligned} \langle A \rangle_W =& \frac{\sum_c W(c) A(c)}{\sum_c W(c)} = \frac{\sum_c h(c)|W(c)|A(c)}{\sum_c h(c)|W(c)|} \\ =& \frac{[\sum_c h(c)|W(c)|A(c)] \,/\, \sum_c |W(c)|}{[\sum_c h(c)|W(c)|] \,/\, \sum_c |W(c)|} \\ =& \frac{\sum_c W'(c)\,[h(c)A(c)]}{\sum_c W'(c)\,[h(c)]} \equiv \frac{\langle hA \rangle_{W'}}{\langle h \rangle_{W'}}, \end{aligned} \tag{2.31}$$

where $W'(c) \equiv |W(c)|$. Therefore, we can use the absolute value as the statistical weight, at the cost of having to divide the averages by the average sign of the product of the fermionic determinants, $\langle \mathrm{sign} \rangle \equiv \langle h \rangle_{W'}$. Whenever $\langle \mathrm{sign} \rangle \sim 1$ the estimate of any physical quantity can be reliably obtained. On the other hand, small values of $\langle \mathrm{sign} \rangle$ introduce strong fluctuations in $\langle A \rangle_W$, thus demanding much longer simulations to reduce fluctuations. It is important to mention that $\langle \mathrm{sign} \rangle < 0.1$ typically leads to a computational cost that renders the simulations impractical. However, recent works have presented numerical evidence that the values of $\langle \mathrm{sign} \rangle$ can be used to track the location of quantum critical points and to estimate the associated critical exponents [74, 75]. Throughout the end of this section, we will discuss how $\langle \mathrm{sign} \rangle$ may provide information about phase transitions.

A phase transition can be characterized by the non-analytic behavior of a specific response function at the critical point. The two-dimensional Ising model provides the simplest example, as the thermal transition to a magnetically ordered phase is accompanied by a divergence in the magnetic susceptibility, exposing the non-analytic behavior of the free energy. Since various observables can be derived from the free energy and the partition function, any non-analyticity in these two quantities is manifested in their derivatives, thus giving information through the response functions.

From Eq. (2.31) we can write $\langle \text{sign} \rangle$ as

$$\langle \text{sign} \rangle = \frac{\sum_c W(c)}{\sum_c |W(c)|} = \frac{\mathcal{Z}_W}{\mathcal{Z}_{W'}}. \tag{2.32}$$

Since the free energy per particle is defined by $f = (\beta N)^{-1} \ln \mathcal{Z}$, the former expression can be rewritten as

$$\langle \text{sign} \rangle = e^{-\beta N (f_W - f_{W'})}. \tag{2.33}$$

Notice that $\sum_c W(c) \leq \sum_c |W(c)|$, so that Eq. (2.33) implies $\mathcal{Z}_W \leq \mathcal{Z}_{W'}$, and then $(f_W - f_{W'}) \geq 0$. With this, it becomes clear from Eq. (2.33) that $\langle \text{sign} \rangle$ decreases with the number of sites and the inverse temperature. Equation (2.33) also shows that $\langle \text{sign} \rangle$ is a composite function of the partition function. In this way, we can expect that a non-analytic behavior of the partition function at any point of parameter space may manifest in $\langle \text{sign} \rangle$, signaling a phase transition.

Chapter 3

The extended Hubbard model on a honeycomb lattice

In this chapter, we discuss the ground state properties of the extended Hubbard model on a half-filled honeycomb lattice. We employ the RHSF and CHSF determinant quantum Monte Carlo approaches to calculate correlation functions and correlation ratios, as well as the double occupancy and the average fermionic sign. With this, we construct the complete $U \times V$ phase diagram, determining the emerging phases and their corresponding phase boundaries.

3.1 SM-AFM transition ($U > 0$)

We start our analysis with the semimetal-antiferromagnetic (SM-AFM) transition. On a half-filled square lattice the HM exhibits AFM order in the ground state for any value of $U > 0$, due to a nested Fermi surface and a van Hove singularity. By contrast, on a half-filled HC lattice, which lacks these properties (the Fermi surface consists of isolated points), the ground state remains semimetallic until a transition to an AFM phase occurs at $(U/t)_c \approx 3.85$ [34, 6]. Since nearest-neighbor repulsion, $V > 0$, favors charge ordering, one expects that $(U/t)_c$ increases with increasing V.

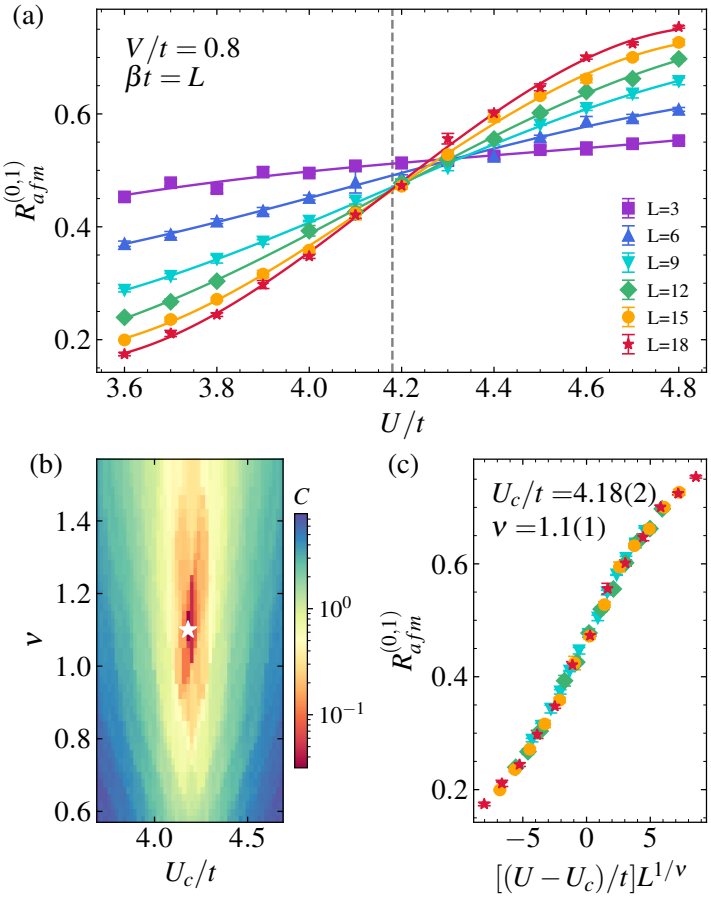

Fig. 3.1: (a) AFM correlation ratio, $R^{(0,1)}_{\rm afm}$, at fixed V as a function of U/t, for different linear system sizes, L. (b) Contour plot of the cost function, C, used to fit $R^{(0,1)}_{\rm afm}$ to a FSS form, Eq. (2.25). The white star locates its minimum, which in turn determines the best fit to the correlation length exponent, ν, and U_c. (c) The resulting FSS data collapse, with fitted ν and U_c; the latter is indicated in (a) by the dashed vertical line.

In order to investigate AFM order in the presence of a finite V, we resort to complex Hubbard-Stratonovich fields to overcome the sign problem for $|V| \leq |U|/3$, as described in Appendix A. Results for the AFM correlation ratio with $\delta^{(0,1)}_{\mathbf{q}}$ are depicted in Fig. 3.1(a): for each pair of successive L's, $R_{\rm afm}$ cross at slightly different values of U. A closer look at the data in Fig. 3.1(a) reveals that for $L < 12$ the crossing points display some size dependence, unlike the data for $L \geq 12$; more on this below. We should mention that the situation is similar for $\delta^{(1,1)}_{\mathbf{q}}$, with the crossing points spanning across a slightly wider range of values; nonetheless, data for the largest L's provide estimates very close to those

obtained from $\delta_{\mathbf{q}}^{(0,1)}$. A precise estimate of U_c can be obtained by invoking the FSS form, Eq. (2.25), to plot the data in Fig. 3.1(a), but now as a function of $(U - U_c)L^{1/\nu}$, with the values of U_c and ν being determined from the minimization of the cost function, C [76]; see Fig. 3.1(b). The resulting data collapse for $V/t = 0.8$ is shown in Fig. 3.1(c), which yields $U_c/t = 4.18 \pm 0.02$ and $\nu = 1.1 \pm 0.1$. This value of U_c practically coincides with the crossing points of $R_{\rm afm}^{(0,1)}$ for $L \geq 12$. The estimate for ν is consistent with the ground state SM-AFM transition for both the HM and the EHM on a half-filled HC lattice belonging to the universality class of the Gross-Neveu model [77, 78, 34, 73, 6, 79]. This correspondence also leads to a dynamical critical exponent $z = 1$ [80]. Given that $z = s/\nu$, with s being the gap exponent [80, 81, 82], we may expect $s = 1$. We have carried out similar analyses of the crossing points for other combinations of U and V to obtain the whole SM-AFM critical line drawn through the (blue) pentagons in Fig. 3.6.

3.2 CDW transitions

In addition to antiferromagnetism, the EHM is expected to display CDW order above some critical curve $V_c(U) > 0$, whose shape we will now determine. From the outset, we note that the search for CDW order should extend beyond the sign-free region, so that for $|V| > |U|/3$ we use real HS fields and monitor the behavior of $\langle \text{sign} \rangle$. Figures 3.2 (a)-3.2 (c) show typical plots for $R_{\rm cdw}$ as a function of V for increasing values of $U \geq 0$; in each panel, data for different system sizes are displayed, whose crossing points provide estimates for the critical values of V. We note that, although these points lie outside the sign-free region, the calculated averages for $U/t \leq 2$ are not degraded, as indicated by the small error bars. To reinforce the accuracy of our estimates, in Fig. 3.2 (d) we show the double occupancy, $\langle D \rangle \equiv \langle n_{\mathbf{i}\uparrow} n_{\mathbf{i}\downarrow} \rangle$ as a function of V, for the same U as in Fig. 3.2 (c); being a local quantity, $\langle D \rangle$ is less sensitive to both noisy $\langle \text{sign} \rangle$ and system size. The transition to a CDW state may take place around $\langle D \rangle = 0.25$, the non-interacting value [83, 84, 37], which in this case occurs at $V_c/t = 0.925 \pm 0.025$ (error estimated by the grid

of values of V used). In addition, Fig. 3.2 (e) shows that while $\langle \text{sign} \rangle$ dips, the $\langle D \rangle$ data in Fig. 3.2 (d) do not degrade, and the dip in $\langle \text{sign} \rangle$ sharpens very close to the estimated critical point [74, 75, 2].

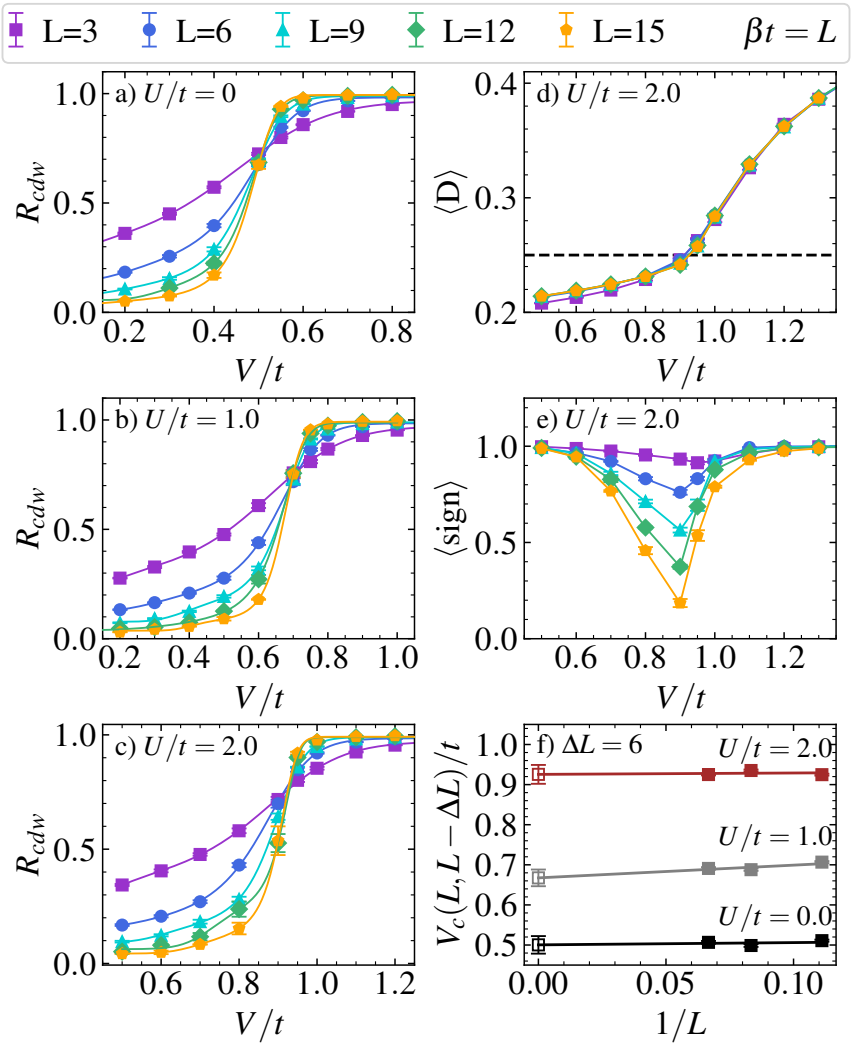

Fig. 3.2: (a)-(c) Charge-density wave correlation ratio for different system linear sizes, L, as a function of V/t, for fixed U. (d) Double occupancy for $U/t = 2$, where the dashed horizontal line indicates the non-interacting value, $\langle D \rangle = 0.25$; see text. (e) Average sign of the product of fermionic determinants for $U/t = 2$. (f) FSS plots of the crossing points (filled squares) in (a)-(c) using sizes L and $L - \Delta L$, with $\Delta L = 6$, leading to the extrapolated values (empty squares) $V_c/t = 0.50 \pm 0.02$, $V_c/t = 0.67 \pm 0.02$ and $V_c/t = 0.92 \pm 0.02$, respectively.

A third and thorough determination of the existence of CDW critical points is given by the crossings of its correlation ratio [37], provided in Figs. 3.2 (a)-3.2 (c). By defining

$V_c(L, L-\Delta L)$ as the crossing of $R_{\rm cdw}(L)$ and $R_{\rm cdw}(L-\Delta L)$, with $\Delta L = 6$, one may extrapolate such crossings to the thermodynamic limit, as displayed in Fig. 3.2 (f). We have performed similar analyses in the second quadrant, $U < 0, V > 0$, and we note that V_c for CDW vanishes at $U/t = -3.85$; more on this below. The points we have obtained for $U/t < 3$ appear as (red) squares in Fig. 3.6.

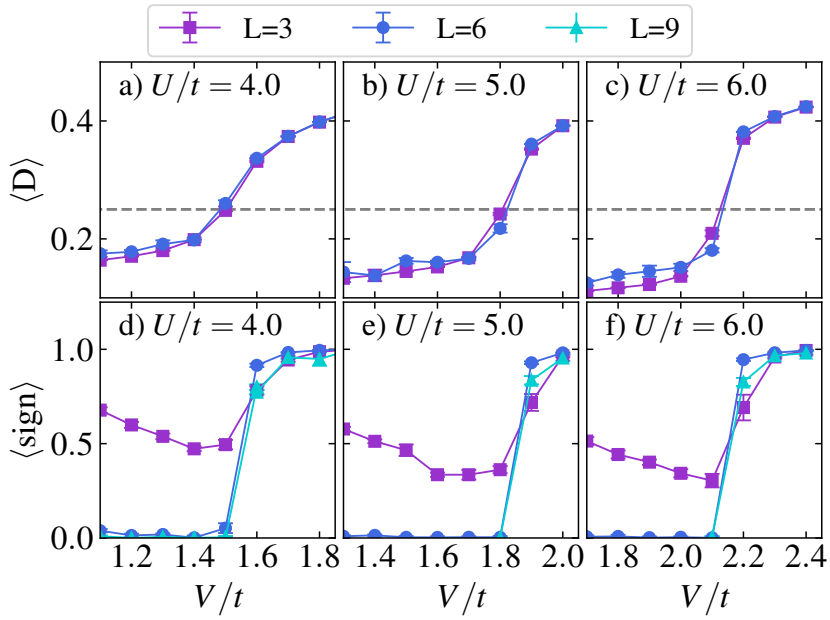

Fig. 3.3: Double occupancy as a function of V for (a) $U/t = 4$, (b) $U/t = 5$ and (c) $U/t = 6$. The dashed horizontal lines correspond to $\langle D \rangle = 0.25$. Average determinant sign and a function of V for (d) $U/t = 4$, (e) $U/t = 5$ and (f) $U/t = 6$. As the system enters the CDW phase, $\langle \text{sign} \rangle$ rises sharply.

For $V > U/3$, $\langle \text{sign} \rangle$ decreases as U is increased beyond $U/t = 2$; this leads to noisy correlation ratios, to the point of precluding finite-size scaling analyses of critical points. However, as discussed above, $\langle D \rangle$ is less sensitive to both $\langle \text{sign} \rangle$ and L, so that data for $L \leq 6$ in this region can still provide reliable estimates for V_c, especially since $\langle D \rangle \lesssim 0.25$ in the AFM state. Figures 3.3 (a)-(c) show the double occupancy for different values of U, from which we see that $\langle D \rangle$ crosses 0.25 at points which hardly depend on L. A totally independent analysis of the transition is provided by the recent observation that a sharp decrease of $\langle \text{sign} \rangle$, calculated with real HS fields, can be used to locate quantum critical

points [74, 75, 85]; this behavior of ⟨sign⟩ at critical points follows from the non-analiticity of the calculated partition function itself [74, 75]. Indeed, Figures 3.3 (d)-(f) display ⟨sign⟩ for the same values of U as in the upper panels: the points where ⟨sign⟩ changes abruptly reproduce with very good accuracy those where $\langle D \rangle = 0.25$. The CDW critical points thus obtained appear as (orange) triangles in Fig. 3.6.

3.3 SM-SC transition

Another consequence of the HC lattice being bipartite is that the HM is particle-hole symmetric; therefore, under a spin-down particle-hole transformation with $V = 0$, the AFM phase at half filling is mapped onto a half-filled $U < 0$ HM in which CDW and superconductivity are degenerate [86, 87, 88]. Thus, s-wave superconductivity occurs at the mirrored region, i.e., for $U/t \lesssim -3.85$ when $V = 0$.

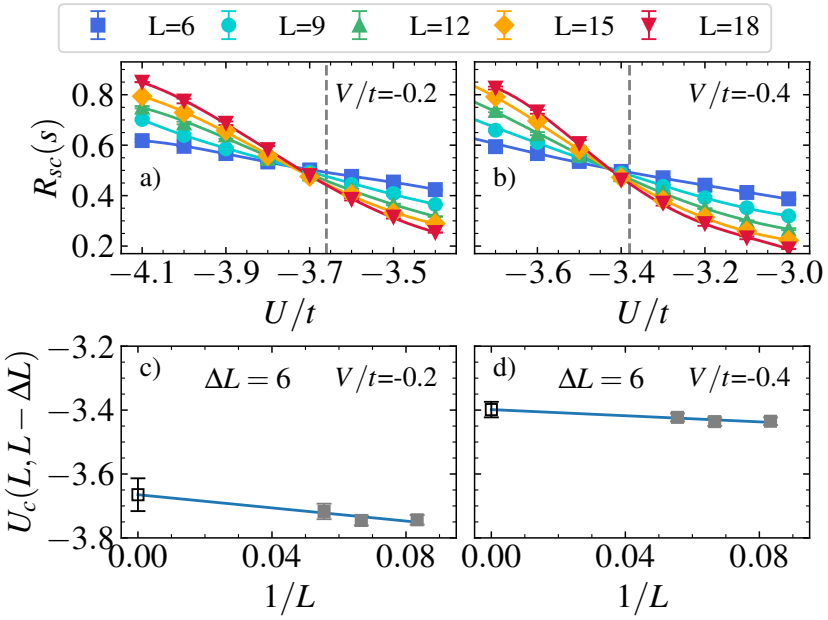

Fig. 3.4: (a) SC correlation ratio as a function of U for $V/t = -0.2$; (b) same as (a), but for $V/t = -0.4$; (c) FSS plot of the crossing points (filled squares) in (a) using sizes L and $L - \Delta$, with $\Delta L = 6$, leading to the extrapolated ($L \to \infty$) value $U_c/t = -3.67 \pm 0.05$ (empty square), indicated by the vertical dashed line in (a); (d) same as (c), but for the data in (b), leading to the extrapolated value $U_c/t = -3.39 \pm 0.02$ respectively.

For any positive (negative) value of V, this degeneracy is broken and the system stabilizes a CDW (superconducting, SC) state. More specifically, when $V < 0$ we expect an enhancement of pair formation, which, in turn, leads to smaller critical values of $|U|$ needed to induce the SC transition. In order to investigate the superconducting phase boundary $U_c(V)$, we resort to complex HS fields for $|V| \leq |U|/3$, and consider lattices up to $L = 18$. Figures 3.4 (a) and 3.4 (b) show the s-wave $R_{\rm sc}$ as a function of U for different fixed values of V. Similarly to the previous CDW case, we determine the SC critical U_c by examining the crossings of $R_{\rm sc}$ for L and $L - \Delta L$, with $\Delta L = 6$ to decrease finite-size effects [37]; the data for U_c thus obtained are then extrapolated to $L \to \infty$, as shown in Figs. 3.4 (c) and 3.4 (d). We have used the same procedure for other values of V (not shown) to obtain the critical curve shown as (purple) circles in Fig. 3.6.

We have calculated several other possible pairing structure factors, described by different form factors; see, e.g., Refs. [35, 62, 63]. However, we have found no evidence for dominance of any pairing symmetry apart from s-wave; see Ref. [2] for similar analyses. This is in marked contrast with what happens for the square lattice, in which case d-wave pairing is stabilized near the non-interacting region [2]. We again attribute this difference to the 'exclusion' of all ordered phases due to the lack of nesting and van-Hove singularity for the half-filled HC lattice.

3.4 Phase separation

For sufficiently strong nearest neighbor attraction, $V < 0$, and over a wide range of values of U, fermions tend to form clusters of doubly occupied nearest neighbor sites. This has a high degeneracy, and is known as a phase separated (PS) phase; it also occurs on the square lattice [2]. As discussed in Refs. [89, 2], one of the features of the PS state is the divergence of the compressibility, due to strong fluctuations in the electronic density, as displayed in Fig. 3.5 (a); it is also manifest in the double occupancy, shown in Fig. 3.5 (c). Since the PS ground state is formed by linear combinations of states with

$n = 0$ and $n = 2$, the staggered CDW structure factor drops to zero within the PS region, as shown in Fig.3.5 (b). Interestingly, $\langle \text{sign} \rangle$ also indicates the PS transition through a sharp minimum near $V/t \sim -0.95$, for $U = 0$. By collecting data for different values of U, we map out the whole PS boundary represented by (green) hexagons in Fig. 3.6.

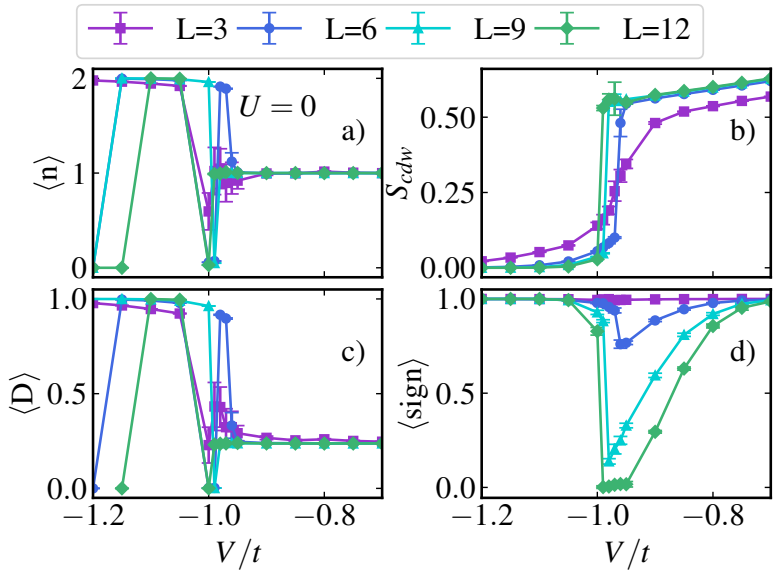

Fig. 3.5: (a) Average density, (b) CDW structure factor (c) double occupancy, and (d) average sign of fermionic determinants, as functions of V/t. All data shown are for $U = 0$.

3.5 Ground state phase diagram

Our findings for the ground state properties of the EHM on a half-filled HC lattice are summarized in the phase diagram of Fig. 3.6. We recall that the HM (i.e., $V = 0$) on the same lattice displays three phases, tunable through the strength and sign of the on-site interaction: s-wave superconducting coexisting with CDW order, for $U/t \lesssim -3.85$; semi-metallic for $-3.85 \lesssim U_c \lesssim 3.85$; and antiferromagnetic for $U_c \gtrsim 3.85$. That is, the absence of nesting and a van Hove singularity at half filling prevents the formation of CDW+SC and AFM states; for comparison, we note that for the square lattice, any $U > 0$ gives rise to an AFM state, while any $U < 0$ gives rise to the degenerate SC and CDW states [2]. This also occurs when a nearest-neighbor repulsion is added: a purely CDW state is only

formed for any $V > 0$ above the SC state; for $U \gtrsim -3.85$ the CDW state is only formed above a critical curve $V_c(U)$. We also note that increasing V requires larger values of U to stabilize the AFM state; at the same time, for sufficiently large U, a direct transition between AFM and CDW takes place, without the need to go through an intermediate SM phase; through the current accuracy of our data, we may expect this to occur for $U/t \gtrsim 6$. For the square lattice, when $U < 0$ a CDW state is formed for any $V > 0$, and above some critical curve. Interestingly, for both lattices the critical curve for $U/t \gg 1$ is very close to the strong coupling prediction for the AFM-CDW transition, $V_c = U/z$, where z is the coordination number, which, in addition, corresponds to the boundary of the sign-free region for both lattices, even in the small U region.

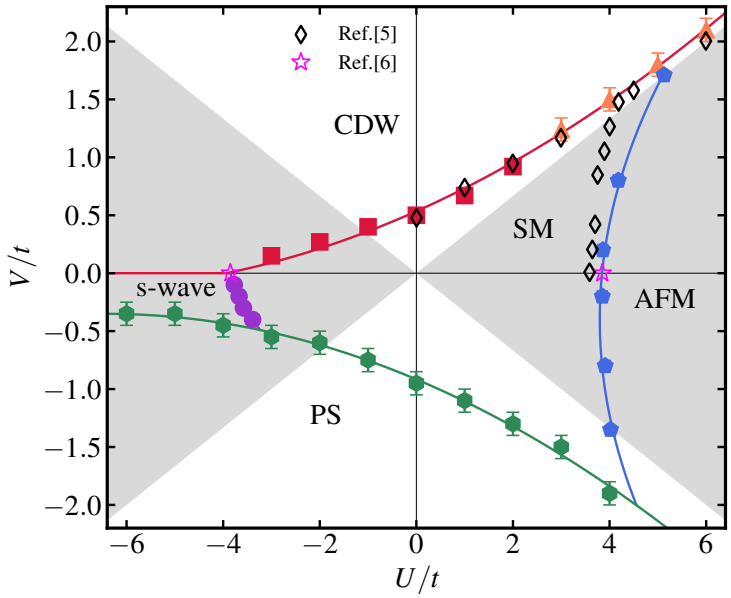

Fig. 3.6: Ground state phase diagram for the Extended Hubbard model on a half-filled honeycomb lattice. Filled symbols are estimates for critical points obtained through our DQMC simulations: (orange) triangles represent results from double occupancy, while (red) squares, (blue) pentagons, and (purple) circles are derived from correlation ratio data. The PS transition points, shown in (green) hexagons, are determined from density, charge structure factor, double occupancy, and $\langle \text{sign} \rangle$. Empty symbols are critical point estimates from DCA (diamonds, Ref. [5]), and from QMC (stars, Ref. [6]). The $|V| \leq |U|/3$ region (shaded) yields sign-free simulations. Lines through data points are guides to the eye.

The 'exclusion' of all ordered phases near the non-interacting region also occurs in the

$V < 0$ half-plane, being bounded below by a PS region. In the $U < 0$ region, the s-wave superconducting phase extends to $V < 0$, with $|U_c(V)/t|$ decreasing slightly from -3.85; see the (purple) circles in Fig. 3.6. However, no change in the symmetry of the paired state was observed: superconductivity is simply suppressed as U is increased, again in marked contrast with the square lattice [2]. Similarly to what happens in the $V > 0$ half-plane, the AFM and PS boundaries seem to merge near $(U, V) \approx (4.2, -2.0)$.

As mentioned before, all previous studies concentrated on the first quadrant [5, 35, 36]. Results from Dynamical Cluster Approximation [5] for the SM-CDW and SM-AFM transitions are included in Fig. 3.6 for comparison; those from Ref. [35] are very close to the former. The agreement with our estimates is very good, although our SM-AFM line is slightly displaced towards larger values of U.

The content of this chapter is part of Ref. [90].

Chapter 4

Concluding remarks

We have studied the extended Hubbard model on a half-filled honeycomb lattice through determinant quantum Monte Carlo simulations, with the aid of structure factors characterizing the possible ordered phases. The 'minus-sign problem' in the region $|V| \leq |U|/3$ was avoided with the use of complex Hubbard-Stratonovich auxiliary fields; when necessary, in other regions we have additionally used the double occupancy, and the actual average sign of the product of fermionic determinants. Employing careful extrapolations towards zero temperature and to the thermodynamic limit (with the aid of finite-size scaling) we have proposed a ground state phase diagram covering the whole (U, V) plane, including the hitherto unexplored domains of attractive interactions, $U < 0$ and/or $V < 0$.

We have established that the lack of nesting and of a van Hove singularity at half-filling produces an 'exclusion' region around the non-interacting limit, $U = V = 0$, in which no ordered phase is stabilized; this exclusion region corresponds to a semi-metallic (SM) phase, due to the presence of Dirac cones. Nonetheless, ordered phases may be stabilized beyond critical boundaries. For instance, in the $V > 0$ region we have obtained the critical line running across $U < 0$ and $U > 0$, above which a charge density wave state may be found.

Interestingly, while for the square lattice one finds two distinct superconducting regions in the $V < 0$ half-plane, namely s- and d-wave pairing states, here only s-wave can be stabilized, and restricted to the $U, V < 0$ quadrant; we have examined the behavior

of other pairing states, but found that they were suppressed as $T \to 0$ for any set of parameters. For sufficiently strong $V < 0$ the system exhibits phase separation.

In the $U > 0$ half-plane, one finds an antiferromagnetic (AFM) critical line, which asymptotically ($V \approx U/3$ with $U/t \gtrsim 6$) meets the charge density wave (CDW) line when $V > 0$; in this $U, V > 0$ region, our phase diagram is similar to the one for the Hubbard-Holstein model on a honeycomb lattice [37], thus illustrating a qualitative similarity between the effects of extended electronic interaction and electron-phonon coupling on the properties of honeycomb-based compounds. Still in this $U > 0$ half-plane, but with $V < 0$, the AFM boundary meets the PS phase. By extending the analysis to both repulsive and attractive interactions, our results help to bridge a gap in the literature regarding the phase diagram of the Hubbard model on the honeycomb lattice.

Appendix A

Complex Hubbard-Stratonovich fields

As discussed in Sec. (2.1), in order to express the (quartic) interaction terms in a quadratic form we employ a Hubbard-Stratonovich transformation. In Eq. (2.3) we defined a real Hubbard-Stratonovich fields (RHSF) transformation. When one uses RHSF for the EHM on a bipartite lattice, even with particle-hole symmetry we suffer from the minus-sign problem. Now we present a complex Hubbard-Stratonovich fields (CHSF) transformation which rises as an alternative to alleviate the minus-sign problem [91, 13, 2]. To start our discussion let us rewrite the interaction terms in Eq. (2.14) as

$$\mathcal{H}_I = \frac{g}{2}\sum_{\langle \mathbf{i},\mathbf{j}\rangle}\left[(n_{\mathbf{i}}-1)+a(n_{\mathbf{j}}-1)\right]^2 = \frac{g}{2}\sum_{\langle \mathbf{i},\mathbf{j}\rangle}\Gamma^2_{\mathbf{i},\mathbf{j}} \tag{A.1}$$

with, $a = V/g$ and $g = 2U/(z + za^2)$. To ensure the correspondence between Eq. (2.14) and Eq. (A.1), a must to be a real solution of the equation

$$2Va^2 - \frac{4Ua}{z} + 2V = 0, \tag{A.2}$$

where z is the coordination number, $z = 3$ for the honeycomb lattice. This requirement is only satisfied if

$$|V| \leq \frac{|U|}{z}. \tag{A.3}$$

Therefore, the calculations with CHSF approach are restricted to this range of interaction parameters.

Now we can perform the HS transformation directly

$$e^{-\Delta\tau g\Gamma^2_{\mathbf{i},\mathbf{j}}/2} = \sum_{\nu=\pm1,\pm2} \eta(\nu) e^{\lambda_\nu \sqrt{-g\Delta\tau}\Gamma_{\mathbf{i},\mathbf{j}}} + \mathcal{O}(\Delta\tau^4), \tag{A.4}$$

where, $\eta(\pm1) = (1 + \sqrt{6}/3)/4$, $\eta(\pm2) = (1 - \sqrt{6}/3)/4$, $\lambda_{\pm1} = \pm\sqrt{3 - \sqrt{6}}$ and $\lambda_{\pm2} = \pm\sqrt{3 + \sqrt{6}}$. This transformation introduces and error of $\mathcal{O}(\Delta\tau^4)$, which is negligible when compared with the Trotter error $\mathcal{O}(\Delta\tau^2)$.

This transformation constrains the relation between up- and down-determinant to only two possible cases. If $g < 0$ the argument of the exponential is real, then the determinants are real and equal. If $g > 0$ the argument of the exponential is purely imaginary, but if there is particle symmetry, the determinants are complex conjugate of each other. In both cases, the product of determinants is a positive definite quantity. Notice that when working with RSHF, there are five fields, each of which can be in two possible states. In contrast, working with CHSF, there is only one field, which can be in four states.

Bibliography

[1] Wing Chi Yu, Shi-Jian Gu, and Hai-Qing Lin. Density matrix spectra and order parameters in the 1d extended Hubbard model. *The European Physical Journal B*, 89(10):212, Oct 2016.

[2] Sebastião dos Anjos Sousa-Júnior, Natanael C. Costa, and Raimundo R. dos Santos. Half-filled extended Hubbard model on a square lattice: Phase boundaries from determinant quantum Monte Carlo simulations. *Phys. Rev. B*, 109:165102, Apr 2024.

[3] K. Sano and Y. Ōno. Critical behavior near the metal-insulator transition in the one-dimensional extended Hubbard model at quarter filling. *Phys. Rev. B*, 70:155102, Oct 2004.

[4] Sebastião dos Anjos Sousa Júnior. *Numerical studies of systems with charge, magnetic and superconducting correlations.* PhD thesis, Universidade Federal do Rio de Janeiro, Rio de Janeiro, 2024.

[5] Wei Wu and A.-M. S. Tremblay. Phase diagram and Fermi liquid properties of the extended Hubbard model on the honeycomb lattice. *Phys. Rev. B*, 89:205128, May 2014.

[6] Yuichi Otsuka, Seiji Yunoki, and Sandro Sorella. Universal quantum criticality in the metal-insulator transition of two-dimensional interacting Dirac electrons. *Phys. Rev. X*, 6:011029, Mar 2016.

[7] J. Hubbard. Electron correlations in narrow energy bands. *Proceedings of the Royal Society of London. Series A, Mathematical and Physical Sciences*, 276(1365):238–257, 1963.

[8] Eduardo Fradkin, Steven A. Kivelson, and John M. Tranquada. Colloquium: Theory of intertwined orders in high temperature superconductors. *Rev. Mod. Phys.*, 87:457–482, May 2015.

[9] Douglas J. Scalapino. The case for d$x^2 - y^2$ pairing in the cuprate superconductors. *Physics Reports*, 250:329–365, 1995.

[10] D. J. Scalapino. A common thread: The pairing interaction for unconventional superconductors. *Rev. Mod. Phys.*, 84:1383–1417, Oct 2012.

[11] Y. Zhang and J. Callaway. Extended Hubbard model in two dimensions. *Phys. Rev. B*, 39:9397–9404, May 1989.

[12] E. Dagotto, J. Riera, Y. C. Chen, A. Moreo, A. Nazarenko, F. Alcaraz, and F. Ortolani. Superconductivity near phase separation in models of correlated electrons. *Phys. Rev. B*, 49:3548–3565, Feb 1994.

[13] Meng Yao, Da Wang, and Qiang-Hua Wang. Determinant quantum Monte Carlo for the half-filled Hubbard model with nonlocal density-density interactions. *Phys. Rev. B*, 106:195121, Nov 2022.

[14] Wei-Chih Chen, Yao Wang, and Cheng-Chien Chen. Superconducting phases of the square-lattice extended Hubbard model. *Phys. Rev. B*, 108:064514, Aug 2023.

[15] D. J. Scalapino, S. R. White, and S. C. Zhang. Superfluid density and the Drude weight of the Hubbard model. *Phys. Rev. Lett.*, 68:2830–2833, May 1992.

[16] Zhuoyu Chen, Yao Wang, Slavko N. Rebec, Tao Jia, Makoto Hashimoto, Donghui Lu, Brian Moritz, Robert G. Moore, Thomas P. Devereaux, and Zhi-Xun Shen.

Anomalously strong near-neighbor attraction in doped 1d cuprate chains. *Science*, 373(6560):1235–1239, 2021.

[17] S. Baier, M. J. Mark, D. Petter, K. Aikawa, L. Chomaz, Z. Cai, M. Baranov, P. Zoller, and F. Ferlaino. Extended Bose-Hubbard models with ultracold magnetic atoms. *Science*, 352(6282):201–205, 2016.

[18] Lin Su, Alexander Douglas, Michal Szurek, Robin Groth, S. Furkan Ozturk, Aaron Krahn, Anne H. Hébert, Gregory A. Phelps, Sepehr Ebadi, Susannah Dickerson, Francesca Ferlaino, Ognjen Marković, and Markus Greiner. Dipolar quantum solids emerging in a Hubbard quantum simulator. *Nature*, 622:724–729, Oct 2023.

[19] Xiqiao Wang, Ehsan Khatami, Fan Fei, Jonathan Wyrick, Pradeep Namboodiri, Ranjit Kashid, Albert F. Rigosi, Garnett Bryant, and Richard Silver. Experimental realization of an extended Fermi-Hubbard model using a 2d lattice of dopant-based quantum dots. *Nature Communications*, 13(1):6824, Nov 2022.

[20] Lucas O. Lima, Andressa R. Medeiros-Silva, Raimundo R. dos Santos, Thereza Paiva, and Natanael C. Costa. Magnetism and metal-insulator transitions in the anisotropic kagome lattice. *Phys. Rev. B*, 108:235163, Dec 2023.

[21] A. Yamada, K. Seki, R. Eder, and Y. Ohta. Mott transition and ferrimagnetism in the Hubbard model on the anisotropic kagome lattice. *Phys. Rev. B*, 83:195127, May 2011.

[22] Yuan Cao, Valla Fatemi, Shiang Fang, Kenji Watanabe, Takashi Taniguchi, Efthimios Kaxiras, and Pablo Jarillo-Herrero. Unconventional superconductivity in magic-angle graphene superlattices. *Nature*, 556:43–50, Apr 2018.

[23] Yuan Cao, Valla Fatemi, Ahmet Demir, Shiang Fang, Spencer L. Tomarken, Jason Y. Luo, Javier D. Sanchez-Yamagishi, Kenji Watanabe, Takashi Taniguchi, Efthimios

Kaxiras, Ray C. Ashoori, and Pablo Jarillo-Herrero. Correlated insulator behaviour at half-filling in magic-angle graphene superlattices. *Nature*, 556:80–84, Apr 2018.

[24] Sung-Hoon Lee, Sungjin Kim, and Kinam Kim. Semimetal-antiferromagnetic insulator transition in graphene induced by biaxial strain. *Phys. Rev. B*, 86:155436, Oct 2012.

[25] Chen Si, Zhimei Sun, and Feng Liu. Strain engineering of graphene: a review. *Nanoscale*, 8:3207–3217, 2016.

[26] Ho-Kin Tang, E. Laksono, J. N. B. Rodrigues, P. Sengupta, F. F. Assaad, and S. Adam. Interaction-driven metal-insulator transition in strained graphene. *Phys. Rev. Lett.*, 115:186602, Oct 2015.

[27] Minsoo Kim, SG Xu, AI Berdyugin, Alessandro Principi, Sergey Slizovskiy, Na Xin, Piranavan Kumaravadivel, Wenjun Kuang, Matthew Hamer, Roshan Krishna Kumar, et al. Control of electron-electron interaction in graphene by proximity screening. *Nat. Commun.*, 11(1):2339, 2020.

[28] Y. I. Joe, X. M. Chen, P. Ghaemi, K. D. Finkelstein, G. A. de la Peña, Y. Gan, J. C. T. Lee, S. Yuan, J. Geck, G. J. MacDougall, T. C. Chiang, S. L. Cooper, E. Fradkin, and P. Abbamonte. Emergence of charge density wave domain walls above the superconducting dome in 1T-$TiSe_2$. *Nature Physics*, 10(6):421–425, Jun 2014.

[29] Sajedeh Manzeli, Dmitry Ovchinnikov, Diego Pasquier, Oleg V. Yazyev, and Andras Kis. 2d transition metal dichalcogenides. *Nature Reviews Materials*, 2(8):17033, Jun 2017.

[30] Alexander Kerelsky, Leo J McGilly, Dante M Kennes, Lede Xian, Matthew Yankowitz, Shaowen Chen, K Watanabe, T Taniguchi, James Hone, Cory Dean,

et al. Maximized electron interactions at the magic angle in twisted bilayer graphene. *Nature*, 572(7767):95–100, 2019.

[31] Javad Vahedi, Robert Peters, Ahmed Missaoui, Andreas Honecker, and Guy Trambly de Laissardière. Magnetism of magic-angle twisted bilayer graphene. *SciPost Phys.*, 11:083, 2021.

[32] Lauro B Braz, George B Martins, and Luis GGV Dias da Silva. Superconductivity from spin fluctuations and long-range interactions in magic-angle twisted bilayer graphene. *Physical Review B*, 109(18):184502, 2024.

[33] Thereza Paiva, R. T. Scalettar, W. Zheng, R. R. P. Singh, and J. Oitmaa. Ground-state and finite-temperature signatures of quantum phase transitions in the half-filled Hubbard model on a honeycomb lattice. *Phys. Rev. B*, 72:085123, Aug 2005.

[34] Fakher F. Assaad and Igor F. Herbut. Pinning the order: The nature of quantum criticality in the Hubbard model on honeycomb lattice. *Phys. Rev. X*, 3:031010, Aug 2013.

[35] J. P. L. Faye, P. Sahebsara, and D. Sénéchal. Chiral triplet superconductivity on the graphene lattice. *Phys. Rev. B*, 92:085121, Aug 2015.

[36] M. Schüler, E. G. C. P. van Loon, M. I. Katsnelson, and T. O. Wehling. First-order metal-insulator transitions in the extended Hubbard model due to self-consistent screening of the effective interaction. *Phys. Rev. B*, 97:165135, Apr 2018.

[37] Natanael C. Costa, Kazuhiro Seki, and Sandro Sorella. Magnetism and charge order in the honeycomb lattice. *Phys. Rev. Lett.*, 126:107205, Mar 2021.

[38] Valeri N. Kotov, Bruno Uchoa, Vitor M. Pereira, F. Guinea, and A. H. Castro Neto. Electron-electron interactions in graphene: Current status and perspectives. *Rev. Mod. Phys.*, 84:1067–1125, Jul 2012.

[39] Michael Golor and Stefan Wessel. Nonlocal density interactions in auxiliary-field quantum Monte Carlo simulations: Application to the square lattice bilayer and honeycomb lattice. *Phys. Rev. B*, 92:195154, Nov 2015.

[40] Hanna Terletska, Sergei Iskakov, Thomas Maier, and Emanuel Gull. Dynamical cluster approximation study of electron localization in the extended Hubbard model. *Phys. Rev. B*, 104:085129, Aug 2021.

[41] Xiao Yan Xu, K. T. Law, and Patrick A. Lee. Kekulé valence bond order in an extended Hubbard model on the honeycomb lattice with possible applications to twisted bilayer graphene. *Phys. Rev. B*, 98:121406, Sep 2018.

[42] Adolfo G. Grushin, Eduardo V. Castro, Alberto Cortijo, Fernando de Juan, María A. H. Vozmediano, and Belén Valenzuela. Charge instabilities and topological phases in the extended Hubbard model on the honeycomb lattice with enlarged unit cell. *Phys. Rev. B*, 87:085136, Feb 2013.

[43] Pedro B. Melo, Sebastião A. S. Júnior, Wei Chen, Rubem Mondaini, and Thereza Paiva. Topological marker approach to an interacting Su-Schrieffer-Heeger model. *Phys. Rev. B*, 108:195151, Nov 2023.

[44] R. Micnas, J. Ranninger, and S. Robaszkiewicz. Superconductivity in narrow-band systems with local nonretarded attractive interactions. *Rev. Mod. Phys.*, 62:113–171, Jan 1990.

[45] Rodrigo A. Fontenele, Natanael C. Costa, Raimundo R. dos Santos, and Thereza Paiva. Two-dimensional attractive Hubbard model and the BCS-BEC crossover. *Phys. Rev. B*, 105:184502, May 2022.

[46] Rodrigo Alves Fontenele, Nathan Vasconcelos, Natanael Carvalho Costa, Thereza Paiva, and Raimundo Rocha dos Santos. Second-neighbor hopping effects in the two-dimensional attractive Hubbard model. *Condensed Matter*, 8(1), 2023.

[47] Rodrigo A. Fontenele, Natanael C. Costa, Thereza Paiva, and Raimundo R. dos Santos. Increasing superconducting T_c by layering in the attractive Hubbard model. *Phys. Rev. A*, 110:053315, Nov 2024.

[48] J. G. Bednorz and K. A. Müller. Possible high-Tc superconductivity in the Ba-La-Cu-O system. *Zeitschrift für Physik B Condensed Matter*, 64(2):189–193, Jun 1986.

[49] J. Bardeen, L. N. Cooper, and J. R. Schrieffer. Theory of superconductivity. *Phys. Rev.*, 108:1175–1204, Dec 1957.

[50] H. Q. Lin, E. R. Gagliano, D. K. Campbell, E. H. Fradkin, and J. E. Gubernatis. *The Phase Diagram of the One-Dimensional Extended Hubbard Model*, pages 315–326. Springer US, Boston, MA, 1995.

[51] Karlo Penc and Frédéric Mila. Phase diagram of the one-dimensional extended Hubbard model with attractive and/or repulsive interactions at quarter filling. *Phys. Rev. B*, 49:9670–9678, Apr 1994.

[52] R. Blankenbecler, D. J. Scalapino, and R. L. Sugar. Monte Carlo calculations of coupled boson-fermion systems. I. *Phys. Rev. D*, 24:2278–2286, Oct 1981.

[53] J. E. Hirsch. Discrete Hubbard-Stratonovich transformation for fermion lattice models. *Phys. Rev. B*, 28:4059–4061, Oct 1983.

[54] J. E. Hirsch. Two-dimensional Hubbard model: Numerical simulation study. *Phys. Rev. B*, 31:4403–4419, Apr 1985.

[55] Naoki Kawashima. Quantum Monte Carlo Methods. *Progress of Theoretical Physics Supplement*, 145:138–149, 02 2002.

[56] Raimundo R. dos Santos. Introduction to quantum Monte Carlo simulations for fermionic systems. *Braz. J. Phys*, 33:63–54, Mar 2003.

[57] R. T. Scalettar, N. E. Bickers, and D. J. Scalapino. Competition of pairing and Peierls–charge-density-wave correlations in a two-dimensional electron-phonon model. *Phys. Rev. B*, 40:197–200, Jul 1989.

[58] Federico Becca and Sandro Sorella. *Quantum Monte Carlo Approaches for Correlated Systems*. Cambridge University Press, 2017.

[59] James Gubernatis, Naoki Kawashima, and Philipp Werner. *Determinant method*, page 180–213. Cambridge University Press, 2016.

[60] Louk Rademaker, Steve Johnston, Jan Zaanen, and Jeroen van den Brink. Determinant quantum Monte Carlo study of exciton condensation in the bilayer Hubbard model. *Phys. Rev. B*, 88:235115, Dec 2013.

[61] A.L. Fetter and J.D. Walecka. *Quantum Theory of Many-particle Systems*. Dover Books on Physics. Dover Publications, 2003.

[62] Xiao Yan Xu, Stefan Wessel, and Zi Yang Meng. Competing pairing channels in the doped honeycomb lattice Hubbard model. *Phys. Rev. B*, 94:115105, Sep 2016.

[63] Tao Ying and Stefan Wessel. Pairing and chiral spin density wave instabilities on the honeycomb lattice: A comparative quantum Monte Carlo study. *Phys. Rev. B*, 97:075127, Feb 2018.

[64] S. R. White, D. J. Scalapino, R. L. Sugar, N. E. Bickers, and R. T. Scalettar. Attractive and repulsive pairing interaction vertices for the two-dimensional Hubbard model. *Phys. Rev. B*, 39:839–842, Jan 1989.

[65] Ribhu K. Kaul. Spin nematics, valence-bond solids, and spin liquids in SO(n) quantum spin models on the triangular lattice. *Phys. Rev. Lett.*, 115:157202, Oct 2015.

[66] Toshihiro Sato, Fakher F. Assaad, and Tarun Grover. Quantum Monte Carlo simulation of frustrated Kondo lattice models. *Phys. Rev. Lett.*, 120:107201, Mar 2018.

[67] Zi Hong Liu, Xiao Yan Xu, Yang Qi, Kai Sun, and Zi Yang Meng. Itinerant quantum critical point with frustration and a non-Fermi liquid. *Phys. Rev. B*, 98:045116, Jul 2018.

[68] Andrew S. Darmawan, Yusuke Nomura, Youhei Yamaji, and Masatoshi Imada. Stripe and superconducting order competing in the Hubbard model on a square lattice studied by a combined variational Monte Carlo and tensor network method. *Phys. Rev. B*, 98:205132, Nov 2018.

[69] Yuichi Otsuka, Kazuhiro Seki, Sandro Sorella, and Seiji Yunoki. Dirac electrons in the square-lattice Hubbard model with a d-wave pairing field: The chiral Heisenberg universality class revisited. *Phys. Rev. B*, 102:235105, Dec 2020.

[70] M. E. Fisher. Critical Phenomena. In M. S. Green, editor, *Proceedings of the Enrico Fermi International School of Physics*, volume 51. Academic Press, New York, 1971.

[71] R. R. dos Santos and L. Sneddon. Finite-size rescaling transformations. *Phys. Rev. B*, 23:3541–3546, Apr 1981.

[72] M. N. Barber. Finite-size scaling. In Cyril Domb and Joel L. Lebowitz, editors, *Phase Transitions and Critical Phenomena*, volume 8, page 145. Academic Press, New York, 1983.

[73] Francesco Parisen Toldin, Martin Hohenadler, Fakher F. Assaad, and Igor F. Herbut. Fermionic quantum criticality in honeycomb and π-flux Hubbard models: Finite-size scaling of renormalization-group-invariant observables from quantum Monte Carlo. *Phys. Rev. B*, 91:165108, Apr 2015.

[74] R. Mondaini, S. Tarat, and R. T. Scalettar. Quantum critical points and the sign problem. *Science*, 375(6579):418–424, 2022.

[75] R. Mondaini, S. Tarat, and R. T. Scalettar. Universality and critical exponents of the fermion sign problem. *Phys. Rev. B*, 107:245144, Jun 2023.

[76] Jan Šuntajs, Janez Bonča, Toma ž Prosen, and Lev Vidmar. Ergodicity breaking transition in finite disordered spin chains. *Phys. Rev. B*, 102:064207, Aug 2020.

[77] David J. Gross and André Neveu. Dynamical symmetry breaking in asymptotically free field theories. *Phys. Rev. D*, 10:3235–3253, Nov 1974.

[78] Igor F. Herbut. Interactions and phase transitions on graphene's honeycomb lattice. *Phys. Rev. Lett.*, 97:146401, Oct 2006.

[79] Ho-Kin Tang, JN Leaw, JNB Rodrigues, IF Herbut, Pinaki Sengupta, FF Assaad, and S Adam. The role of electron-electron interactions in two-dimensional Dirac fermions. *Science*, 361(6402):570–574, 2018.

[80] P. C. Hohenberg and B. I. Halperin. Theory of dynamic critical phenomena. *Rev. Mod. Phys.*, 49:435–479, Jul 1977.

[81] R R dos Santos and R B Stinchcombe. Finite size scaling and crossover phenomena: the XY chain in a transverse field at zero temperature. *Journal of Physics A: Mathematical and General*, 14(10):2741, oct 1981.

[82] R B Stinchombe and R R dos Santos. Critical dynamics of quantum chains by position space renormalisation group. *Journal of Physics A: Mathematical and General*, 18(10):L597, jul 1985.

[83] E. A. Nowadnick, S. Johnston, B. Moritz, R. T. Scalettar, and T. P. Devereaux. Competition between antiferromagnetic and charge-density-wave order in the half-filled Hubbard-Holstein model. *Phys. Rev. Lett.*, 109:246404, Dec 2012.

[84] S. Johnston, E. A. Nowadnick, Y. F. Kung, B. Moritz, R. T. Scalettar, and T. P. Devereaux. Determinant quantum Monte Carlo study of the two-dimensional single-band Hubbard-Holstein model. *Phys. Rev. B*, 87:235133, Jun 2013.

[85] Stefan Wessel, B. Normand, Frédéric Mila, and Andreas Honecker. Efficient Quantum Monte Carlo simulations of highly frustrated magnets: the frustrated spin-1/2 ladder. *SciPost Phys.*, 3:005, 2017.

[86] Hiroyuki Shiba. Thermodynamic Properties of the One-Dimensional Half-Filled-Band Hubbard Model. II: Application of the Grand Canonical Method. *Prog. Theor. Phys.*, 48(6):2171–2186, 12 1972.

[87] V. J. Emery. Theory of the quasi-one-dimensional electron gas with strong "on-site" interactions. *Phys. Rev. B*, 14:2989–2994, Oct 1976.

[88] Raimundo R. dos Santos. Attractive Hubbard model on a triangular lattice. *Phys. Rev. B*, 48:3976–3982, Aug 1993.

[89] G. G. Batrouni and Richard T. Scalettar. Langevin simulations of a long-range electron-phonon model. *Phys. Rev. B*, 99:035114, Jan 2019.

[90] Welberth Kennedy, Sebastião dos Anjos Sousa-Júnior, Natanael C. Costa, and Raimundo R. dos Santos. Extended hubbard model on a honeycomb lattice. *Phys. Rev. B*, 111:155118, Apr 2025.

[91] Michael Golor and Stefan Wessel. Nonlocal density interactions in auxiliary-field quantum monte carlo simulations: Application to the square lattice bilayer and honeycomb lattice. *Phys. Rev. B*, 92:195154, Nov 2015.